ISSN 1849–0751 (On–line)
ISSN 0013–7448 (Print)
UDK 621.31

https://doi.org/10.37798/EN2023723

Journal of Energy

VOLUME 72 Number 3 | 2023

ENERGIJA 72

Journal of Energy

Scientific Professional Journal Of Energy, Electricity, Power Systems
Online ISSN 1849–0751, Print ISSN 0013–7448, VOL 72
https://doi.org/10.37798/EN2023723

Published by
HEP d.d., Ulica grada Vukovara 37, HR–10000 Zagreb
HRO CIGRÉ, Berislavićeva 6, HR–10000 Zagreb

EDITORIAL

The first paper is entitled “Alignment of aFRR and mFRR prequalification process in Croatia with the target market design”. The paper gives an overview of the current prequalification practices of HOPS, examines the PICASSO and MARI standards and evaluates the prequalification processes in Slovenian and German transmission system operators. The prequalification process, as defined in Commission Regulation (EU) 2017/1485, ensures that entities or groups providing reserves meet the requirements of transmission system operators. HOPS, the Croatian Transmission System Operator, carries out this process for potential providers of ancillary services, a prerequisite for offering ancillary services. This paper examines the differences between the existing prequalification rules and the technical requirements in PICASSO and MARI, analyzes the practices in Slovenia and Germany and proposes adjustments for the Croatian aFRR and mFRR prequalification procedures. FCR and RR are excluded. The focus is on aFRR and mFRR as balancing services in Croatia. The conclusion emphasizes the need to adopt the mFRR operational test.

The second paper is “Optimizing Remaining Useful Life Estimation of Lithium-Ion Batteries: A Particle Swarm Optimization-Based Grey Prediction Mode”. This study presents an innovative grey modelling method for predicting the Remaining Useful Life (RUL) of lithium-ion batteries (LIBs). Using the NASA dataset for charge and discharge cycles, the proposed model significantly improves energy storage system dependability and security. By integrating grey system theory and optimization techniques, the approach outperforms existing Grey modelling methods in terms of accuracy and computational efficiency. The study also suggests the inclusion of factors such as current, voltage and temperature to further improve the accuracy of RUL prediction. The research emphasizes the crucial need for accurate estimation of the age and condition of LIBs, taking into account environmental and usage factors. The study helps to ensure the reliability and safety of LIBs and represents a significant advance in RUL prediction for practical applications.

The third paper is entitled “Development of transformers with natural ester and cellulose or aramid insulation”. This study deals with research work aimed at establishing design guidelines for power transformers utilizing natural esters. The presented simulation results confirm the appropriateness of the design rules and allow the necessary adjustments for the implementation of the new insulation system compared to the traditional mineral oil and cellulose based solid insulation. The results also serve as a basis for the subsequent design of transformers that combine natural esters with aramid insulation. The development of advanced transformers with alternative insulation systems required a comprehensive analysis of material integration into the design. The research is a decisive step towards advancing transformer design for improved efficiency and sustainability.

The fourth article is “Development of Fiber Reinforced Compound Bipolar Foils for Fuel Cells”. The research project »InduRex« focused on the production of graphite polymer bipolar plates with minimal thickness, aligning with the » Department of Energy« standards. The project successfully translated a metallic bipolar plate design to a compound foil, but concerns about reduced mechanical stability with larger foils prompted the introduction of carbon fibers in the »Faserverstaerkte Folien« research project. Continuous production of highly filled foils was achieved, which were successfully structured as bipolar foils for fuel cell operation. Initial cell tests showed good efficiency at different current densities, motivating the ongoing pursuit of creating bipolar plates from compound foils. The current challenge is to produce larger active area bipolar films with increased mechanical stability for constructing multicell stacks. The studies carried out show that the area-specific forward resistances of the most electrically conductive bipolar foils are below 20 mΩ in the unstructured state.

The last paper is “Simulated Thermal Fault: Assessing Dissolved Gas Analysis through Tube Heating Method on Mineral Oils and Natural Ester”. This study presents a test system developed for the investigation of thermal faults using the tube heating method, an essential technique for early fault detection and transformer condition monitoring. In the study, the Tube Heating Technique is used to simulate thermal faults at temperatures up to 800 °C and to investigate the variations of dissolved gases depending on the fault severity and the type of insulating liquid. DGA data from commercially available insulating fluids, including inhibited and uninhibited mineral oils and a natural ester, demonstrate differences in gas formation. Examination of an inhibited mineral oil, an uninhibited mineral oil and a natural ester using the tube heating method at temperatures up to 800 °C showed similar gas levels for mineral oils, but significantly higher carbon monoxide and carbon dioxide levels for the natural ester.

Igor Kuzle
Editor–in–Chief

Journal of Energy

VOLUME 72 Number 3 | 2023

journal homepage: http://journalofenergy.com/

Alignment of aFRR and mFRR prequalification process in Croatia with the target market design

Petra Sagrestano Štambuk, Dajana Vrbičić Tenđera, Nikolina Zovko, Tomislav Tenđera and Marin Uzelac

***Summary* — Commission Regulation (EU) 2017/1485 of 2 August 2017 establishing a guideline on electricity transmission system operation defines a prequalification process as a process to verify the compliance of a reserve providing unit or a reserve providing group with the requirements set by the transmission system operator. Croatian Transmission System Operator Plc. (HOPS) carries out a prequalification process in order for (potential) ancillary service providers to prove their capability of providing ancillary services, which means that the prequalification process is a prerequisite for the provision of ancillary services. As part of the European Network of Transmission System Operators for Electricity, HOPS participates in the European implementation projects PICASSO and MARI, which aim is to establish a single European platform for aFRR and mFRR balancing services. Within the PICASSO and MARI projects, the technical characteristics of the products traded on unique European platforms were defined. This paper analyzes the difference between the requirements from the existing prequalification process rules and the technical requirements for products within the PICASSO and MARI projects, explores practice in Slovenia and Germany and suggests the required adoptions of aFRR and mFRR prequalification process in Croatia.**

***Keywords* — aFRR, MARI, mFRR, PICASSO, prequalification process**

I. Introduction

ANCILLARY services refer to a range of functions which transmission system operators (TSOs) contract so that they can guarantee system security. [1]

Croatian Transmission System Operator Plc. (HOPS) is the independent TSO in Croatia. HOPS determines the types, scope of supply, providers and period of supply of ancillary services. The Electricity Market Act (Official Gazette 111/2021) divides ancillary services into balancing services and non-frequency ancillary services. In European practice, balancing services are also called frequency ancillary services.

Frequency ancillary services in Europe are divided into four main reserve categories: Frequency Containment (FCR), automatic (aFRR) and manual (mFRR) Frequency Restoration, and Replacement Reserve (RR). The FCR and aFRR are automatically activated reserves (activated upon a frequency deviation) with fast response and short but more frequent activation events. The mFRR and RR are manually activated reserves with slower response, longer and less frequent activation events. FCR is used to intervene automatically within seconds in the entire synchronous area to restore the balance between the supply and the demand. A provider must be able to ramp up/down its generation/consumption to the full power within 30 seconds after a disturbance. After successful FCR activation, the frequency is at a stable value below or above the nominal value. The task of restoring the frequency to its nominal value is performed by aFRR and, if necessary, additionally by mFRR. The aFRR acts on a Load Frequency Control (LFC) area level where it replaces local FCR activations and mitigates power flow imbalances on the LFC interconnection lines. The activation time for aFRR provision is 30 seconds to 7.5 minutes in Europe (5 minutes after 2024). The mFRR is manually activated to release the activated aFRR capacity or to provide additional frequency restoration power [2]. At the time of writing the paper, full activation time of mFRR in HOPS control area is 15 minutes while in most European countries is 12.5 minutes. As the mFRR provision is gradually increasing, the aFRR is released and can be used for new imbalances. Additionally, a TSO can use RR, but is not obligatory. Full activation time of RR is 30 minutes.

In Table I the comparison between frequency ancillary services is shown. It should be noted that full activation time for aFRR and mFRR may vary within European countries. Harmonization of full activation times at the European level is expected in the framework of common implementation projects.

TABLE I

Comparison Between Frequency Ancillary Services

	Full activation time	Activation	Purpose
FCR	30 seconds	Automatically activated	Frequency containment
aFRR	5 minutes*	Automatically activated	Frequency restoration
mFRR	12,5 minutes*	Manually activated	Frequency restoration
RR	30 minutes	Manually activated	Frequency restoration

*may vary within European countries

FCR and RR are out of the scope of this paper. In Croatia, at the time of writing this paper, aFRR and mFRR are considered as balancing services. All individual network users and aggregators who have signed Balancing Service Agreement with HOPS can provide balancing services. A prerequisite for signing Balancing Service Agreement is successfully completion the prequalification process and proof of technical ability to provide balancing services.

(Corresponding author: Petra Sagrestano Štambuk)

Petra Sagrestano Štambuk, Dajana Vrbičić Tendera, Nikolina Zovko, Tomislav Tenđera and Marin Uzelac are with the Croatian Transmission System Operator Plc. (HOPS d.d.) Zagreb, Croatia

(e-mails: petra.sagrestanostambuk@hops.hr, dajana.vrbicic-tendera@hops.hr, nikolina.zovko@hops.hr, tomislav.tendera@hops.hr and marin.uzelac@hops.hr)

Petra Sagrestano Štambuk, Dajana Vrbičić Tenđera, Nikolina Zovko, Tomislav Tenđera and Marin Uzelac, Alignment of aFRR and mFRR prequalification process in Croatia with the target market design, Journal of Energy, vol. 72 Number 3 (2023), 3–7
https://doi.org/10.37798/2023723472

II. Prequalification Process Rules

In accordance with Commission Regulation (EU) 2017/1485 of 2 August 2017 establishing a guideline on electricity transmission system operation, HOPS has developed document Rules for conducting prequalification process (Verification process for provision of aFRR and mFRR balancing services) that was valid at the time of writing this paper. The document defines the procedure for performing aFRR and mFRR prequalification process, the steps of which are listed below. The first step in prequalification process is the application process. When applying for the prequalification process, the candidate submits a completed Application form for aFRR or mFRR balancing service. HOPS checks submitted forms and if the criteria are met, informs the candidate about the possibility of continuing the prequalification process. The second step is testing the communication systems, which needs to be completed before proceeding to the final step, which is testing the technical capability to provide aFRR or mFRR balancing services. The requirements that are tested in the last step are listed in the documents Test profiles for aFRR service and Test profiles for mFRR service which are available on HOPS' website. After the completion of the last step, HOPS evaluates the results of the prequalification process [4].

A. aFRR operating test

Operating test for aFRR balancing service includes the following steps:

1) upper and lower limits of control range check,
2) verifying declared gradient (ramping) for positive and negative direction,
3) dead band between two opposite requests check and
4) checking operation in the middle of the control range and response to small changes check.

In coordination with a candidate, HOPS creates a detailed test program for each test. Requirements regarding a candidate's response are shown in Figure 1. Reaction time needs to be less or equal to 30 seconds and full activation time up to 5 minutes [5].

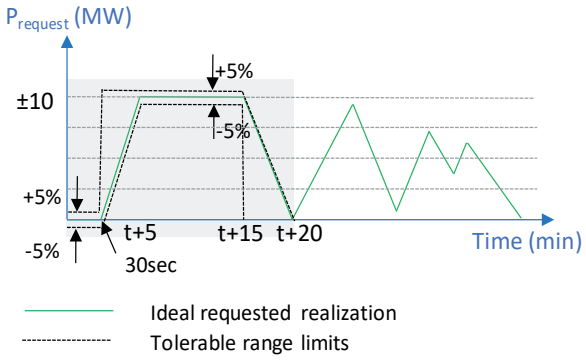

Fig. 1. aFRR operating test [5]

B. mFRR operating test

When testing the technical ability to provide the mFRR balancing service, the candidate proves his ability by responding to two activation requests. Activation requests and allowable response limits are shown in Figure 2. The first activation request lasts 30 minutes, while the second activation request lasts 75 minutes. The interval between activation requests is arbitrarily determined by HOPS during testing, respecting the minimum period between activation requests of 15 minutes and taking into account the deactivation time of the previous activation request. The maximum time between activation requests is 300 minutes.

Requirements regarding response are shown in Figure 2. [6]

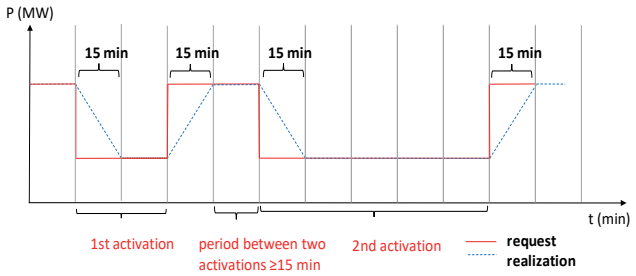

Fig. 2. mFRR operating test [6]

As it is shown in Figure 2, the criteria for full activation time is 15 minutes.

III. European Implementation Projects MARI and PICASSO

The Platform for the International Coordination of Automated Frequency Restoration and Stable System Operation (PICASSO) and Manually Activated Reserves Initiative (MARI) are implementation projects of European transmission system operators whose goal is the establishment of European aFRR and mFRR platforms, two key objectives of Commission Regulation (EU) 2017/2195 of November 23, 2017 on the establishment of guidelines for balancing electricity. The purpose of the joint platforms is to improve the efficiency of the balancing process at the European level and integrate the balancing energy market, promote the possibility of exchanging aFRR and mFRR balancing energy while contributing to maintaining operational security. According to the projects' timelines, the connection of HOPS' internal balancing platform with the European aFRR and mFRR platforms is planned for July 2024.

In the context of alignment of the prequalification process with the requirements of European platforms, it is necessary to analyze the products offered on the platforms.

A. aFRR product within PICASSO project

PICASSO project was designed with the aim of connecting the AGC systems of individual TSOs and achieving maximum social benefit at the European level, taking into account the network topology and the balance of bids of aFRR balancing service providers. The AGC system, i.e. the system for automatic regulation of production, is the basic system for carrying out the frequency restoration process using the aFRR balancing service. The network topology is modeled with constraints for each boundary of load-frequency control area. These limits are called Available Transmission Capacities and they are determined by predefined processes. The AGC system of each individual OPS within the PICASSO project should always be connected to the central optimizer (Activation Optimization Function) of the aFRR platform, i.e. with a common priority list. The activation itself takes place in cycles that are activated at intervals of every 4 seconds. Each cycle consists of three steps. The first step is the calculation of the value for the unsatisfied demand (surplus or shortage of energy) of an individual TSO according to the common priority list, the second step is the netting TSO's deviation, and the third step is the recalculation of the value for the unsatisfied demand according to the common priority list. After these three steps, the total prices are calculated depending on the prices of the offers and the limitations of transmission capacities. Activation according to the aFRR platform takes place after each cycle, while the TSO – balancing service provider (BSP) delivery shape is subject to definition at the national level. [7]

Petra Sagrestano Štambuk, Dajana Vrbičić Tenđera, Nikolina Zovko, Tomislav Tenđera and Marin Uzelac, Alignment of aFRR and mFRR prequalification process in Croatia with the target market design, Journal of Energy, vol. 72 Number 3 (2023), 3–7
https://doi.org/10.37798/2023723472

Standard aFRR product has the following characteristics:

1) by December 2024, the full activation time is harmonized to 5 minutes,
2) minimum bid size and the bid granularity are harmonized to 1 MW,
3) the validity period for aFRR bids is harmonized to 15 minutes,
4) all bids are divisible,
5) complex bids/linked bids are not supported by the aFRR platform.

B. mFRR PRODUCT WITHIN MARI PROJECT

Optimization algorithm developed within MARI is formulated as Mixed Integer Linear Programming Problem. The primary objective of the Activation Optimization Function is to maximize social welfare and the secondary objective is the minimization of cross-border exchanges. On the mFRR platform, the standard mFRR product can be ordered either through scheduled activation or direct activation with a minimum quantity of 1 MW. Direct and scheduled activations use the same Activation Optimization Function with different input data. Balancing service providers may choose if their bids are available for direct activations. The exchange shape for scheduled and direct activation between two TSOs is shown in Figure 3. TSO – BSP delivery is defined in the national terms and conditions. Optimization for scheduled activation runs every 15 minutes, once for each 15-minute interval, with delivery for the next 15-minute interval [8].

The full activation time is the same for both scheduled and direct activations and is 12.5 minutes, while 2.5 minutes is the time required for communication between the central and national platforms. The key data for the prequalification process is the full activa

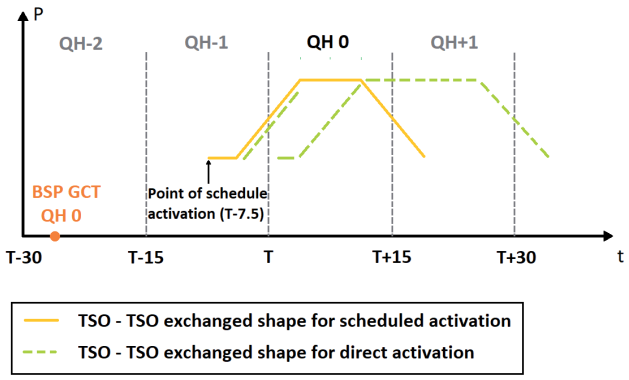

Fig. 3. Scheduled and direct activation within MARI [8]

IV. EXAMPLES OF PREQUALIFICATION PROCESSES OF SOME EUROPEAN TSOS

In order to gain a broader overview of the prequalification processes in Europe, two examples of prequalification processes are presented in this chapter: Slovenian TSO's (ELES) and German TSOs' (Amprion GmbH, TransnetBW GmbH, TenneT TSO GmbH and 50Hertz Transmission GmbH) process.

A. ELES - SLOVENIA

In the document Terms and conditions for balancing service providers on the ELES balancing market aFRR and mFRR, available in English, prequalification processes are defined. The steps of ELES' prequalification process are shown in Figure 4 [9].

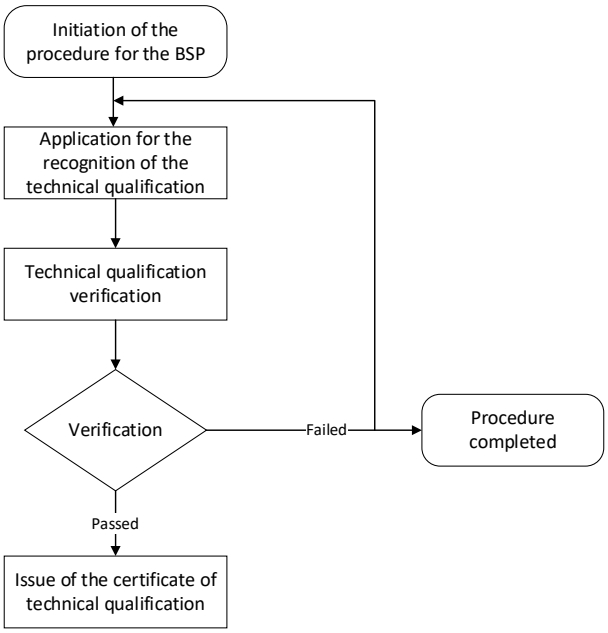

Fig. 4. The steps of ELES' prequalification process [9]

1) TEST ACTIVATION FOR AFRR

The prerequisite for conducting the qualification test is a successful application by sending the "Application for technical qualification of the balance service provider" form and successful testing of communication and information system. In the Article 49 of Terms and conditions for balancing service providers on the ELES balancing market technical requirements for providing aFRR service are stated:

1. The BSP shall be capable of activating or deactivating the total volume of the aFRR balancing energy bid, i.e. they shall be capable of implementing the change of active power from the value of the operating point up to the limit of the offered aFRR volume in no more than five minutes;
2. After a certain time delay (a reaction time of 30 seconds), the activated value shall start following set point, and in no more than five minutes, shall achieve the requested value with an imbalance of 5% of the sum of all aFRR balancing bids submitted by individual BSP being allowed. For a short period of time a single overshoot is allowed in the direction of the activation, namely up to 10 % of the value of the activated balancing capacity with the maximum allowed value of the overshoot being limited to 10 MW.

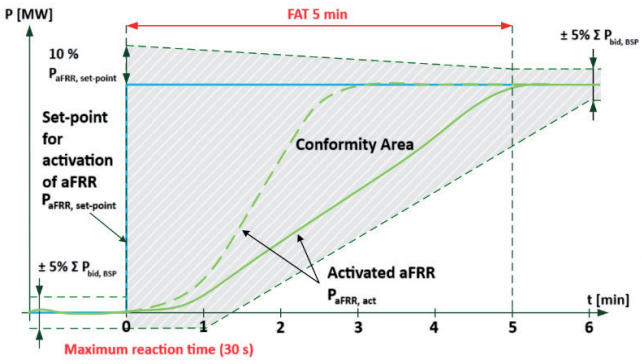

Fig. 5. The range of the response adequacy in the event of a step change of the required balancing capacity [9]

Petra Sagrestano Štambuk, Dajana Vrbičić Tenđera, Nikolina Zovko, Tomislav Tenđera and Marin Uzelac, Alignment of aFRR and mFRR prequalification process in Croatia with the target market design, Journal of Energy, vol. 72 Number 3 (2023), 3–7
https://doi.org/10.37798/2023723472

2) Test activation for mFRR

Just like for the aFRR balancing service, the prerequisite for the performing qualification test for mFRR is a successful application by sending the "Application for technical qualification of the balance service provider" form and successful testing of communication and information system. In article 97. of Terms and conditions for balancing service providers on the ELES balancing market technical requirements for providing aFRR service are stated. The BSP shall be capable of activating the control group or the portfolio which they use to provide the mFRR service, i.e. they shall be capable of changing the active power in accordance with the TSO's requirement, so that they:

1) reach the required value of the capacity within 12,5 minutes of the request being submitted by the TSO and

2) implement the change of the required capacity or end the activation within 12.5 minutes of the request being submitted by the TSO.

As with the aFRR service, two activation tests are performed when testing the mFRR balancing service. Activation test example is in the Figure 6 [9].

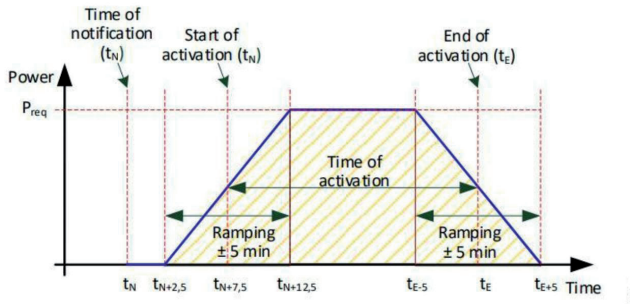

Fig. 6. An example of test activation for mFRR in the framework of the qualification procedure [9]

B. German TSOs

Four TSOs operate in the German control area: Amprion GmbH, TransnetBW GmbH, TenneT TSO GmbH and 50Hertz Transmission GmbH. The document Prequalification Process for Balancing Service Providers (FCR, aFRR, mFRR) in Germany ("PQ conditions"), available in English, defines the requirements that must be fulfilled within the prequalification process, which apply to all four German TSOs.

In the document is stated that prequalification process and prequalification application are carried out via PQ portal. As a part of the application documents, the candidate needs to deliver the required data and results of the carried operating test. The required information technology configuration is described in the separate document that can be found on the official website. The operating test is normally carried out independently by the BSP. Coordination with the reserve connecting TSO is however requested in cases in which a BSP intends to prequalify 150 MW of power or more. However, in the case of prequalification of a power reserve of more than 150 MW, coordination with the competent TSO is required.

The prequalifiable power (actual balancing reserve value of the stationary period) is determined by evaluating the results of the performed operating test according to defined formulas. In addition to the operating test, a control system test is carried out. In contrast to the operating test, which the BSP carries out without the participation of the reserve connecting TSO, the control system test is carried out in close coordination with the TSO. The control system test has two primary elements: The BSP must show that its pool is connected correctly to the control system of the TSO and the BSP must verify the robustness of the providing by the pool [10].

Within the document, all steps within the prequalification process are comprehensively defined, as well as certain specifics that are not included in this paper.

1) aFRR operating test

Within aFRR operating test, the response time up to 30 seconds, the power change period of 5 minutes and a deactivation time of 5 minutes are defined. A stationary period, which starts 5 minutes after the set point change and lasts at least 10 minutes is also defined. Typically, three reservation and two activation phases are carried out during an operating test. Figure 7 shows the permissible and acceptable fluctuations as part of the aFRR operating test [10].

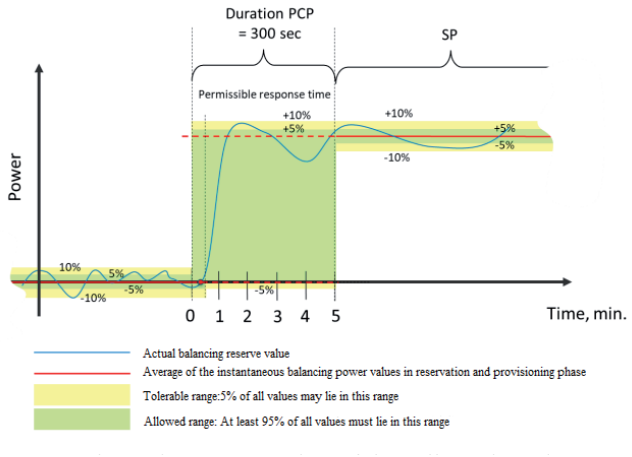

Fig. 7. Schematic representation of the "allowed" and "acceptable" intervals (aFRR) [10]

2) mFRR operating test

In the case of mFRR, the power change period starts with the set point change and ends 12.5 minutes after the set point change. The stationary period starts 12.5 minutes after the set point change. It lasts at least 10 minutes Typically, three reservation and two activation phases are carried out during an operating test. Figure 8 shows the permissible and acceptable fluctuations as part of the aFRR operating test. [9]

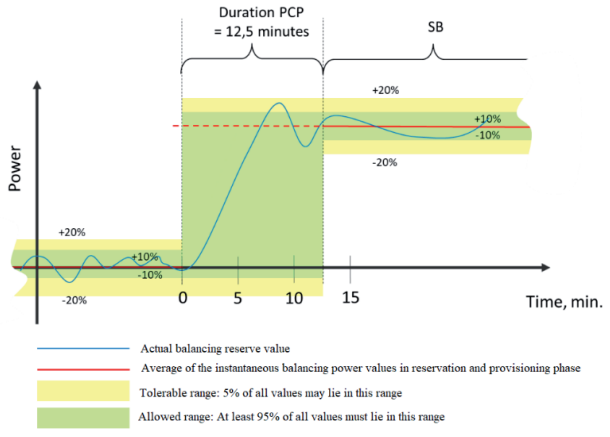

Fig. 8. Schematic representation of the "allowed" and "acceptable" intervals (mFRR) [10]

Petra Sagrestano Štambuk, Dajana Vrbičić Tenđera, Nikolina Zovko, Tomislav Tenđera and Marin Uzelac, Alignment of aFRR and mFRR prequalification process in Croatia with the target market design, Journal of Energy, vol. 72 Number 3 (2023), 3–7
https://doi.org/10.37798/2023723472

C. Compliance of ELES and German TSOs' prequalification process with PICASSO and MARI

When comparing the requirements of the PICASSO and MARI projects with the prequalification processes of ELES and German TSOs, it can be concluded that the prequalification processes are adapted to European implementation projects. This is supported by the fact that German TSOs are already connected to European aFRR and mFRR platforms.

V. Adopting aFRR and mFRR Prequalification Process in Croatia

HOPS is currently adopting the aFRR and mFRR prequalification process. The planned completion and publication of the document is at the beginning of 2024. Unlike the existing version, the new version of the document will be improved in the form of terminology standardization and a clearer structure, in addition, it will be adapted to the requirements of target market design (PICASSO and MARI). During the creation of the new document, the requirements of European implementation projects as well as the existing European practice were analyzed. It was found that mFRR operating test needs to be adjusted. With regard to the performed analyses, it was concluded that the full activation time (time to reach full declared reserved power) must be changed from 15 minutes to 12.5 minutes.

Table II

Comparison Between Full Activation Time in Existing and New aFRR and mFRR Prequalification Process

	Full activation time	
	Existing prequalification process	New prequalification process
aFRR	5 minutes	5 minutes
mFRR	15 minutes	12,5 minutes

Additionally, HOPS considers shortening the duration of the activation, defining the amount of the tolerance threshold and validating the deactivation time. Additionally, given the different requirements compared to current practice, it is necessary to decide which providers must repeat the prequalification process. The considered example of mFRR operating test profile is shown in Figure 9.

The requirements of the aFRR operating test do not need to be changed.

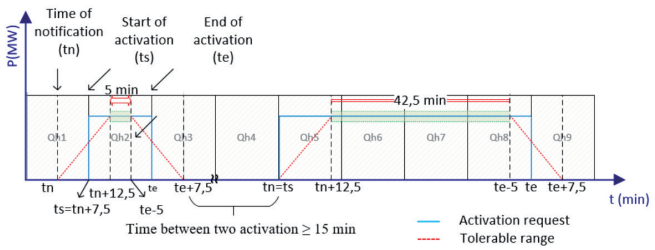

Fig. 9. Potential profile of mFRR operating test

V. Conclusion

PICASSO and MARI projects represent the target market design for aFRR and mFRR balancing services. In order to be able to participate in PICASSO and MARI, some TSOs need to adjust local processes. One of the processes that potentially need to be adopted is the prequalification process for providing aFRR and mFRR balancing services. The paper provides an overview of the existing HOPS' practice of performing aFRR and mFRR prequalification process and in order to determine the necessary changes, it analyses PICASSO and MARI standard products and prequalification processes of Slovenian TSO and German TSOs. To conclude, the mFRR operating test needs to be adopted.

The identified changes, together with other improvements, will be included in a new document which is expected to be finalized and published in early 2024.

References

[1] *"Balancing and Ancillary Services Markets"*, accessed: 20 May 2023., available at link: https://docstore.entsoe.eu/about-entso-e/market/balancing-and-ancillary-services-markets/Pages/default.aspx

[2] I. Pavić, T. Capuder and H. Pandžić, "Analysis of aFRR and mFRR Balancing Capacity & Energy Demands and Bid Curves," *ENERGYCON 2022*, accessed: 10 September 2023., available at link: https://flexibase.fer.hr/images/50036309/Analysis_of_aFRR_and_mFRR_Balancing_Capacity_amp_Energy_Demands_and_Bid_Curves.pdf

[3] *"Commission Regulation (EU) 2017/1485 of 2 August 2017 establishing a guideline on electricity transmission system operation"*, accessed: 30 May 2023., available at link: https://eur-lex.europa.eu/legal-content/HR/TXT/PDF/?uri=CELEX:32016R0679

[4] *"Verification process for provision of aFRR and mFRR balancing services"*, accessed: 1 June 2023., available at link: https://www.hops.hr/page-file/5MllLGiI4a2rSAlL08dVY2/prequalification-process/Verifikacijski_postupak_za_pru%C2%BAanje_usluga_uravnote%C2%BAenja_aFRR_i_mFRR.pdf

[5] *"Test profiles for aFRR service"*, accessed: 1 June 2023., available at link: https://www.hops.hr/page-file/ei0oyf8z55BiDUhrG2BRH3/prequalification-process/TESTIRANJE%20SPOSOBNOSTI%20JEDINICA%20ZA%20PRU%C2%AAANJE%20USLUGE%20aFRR.pdf

[6] *"Test profiles for mFRR service"*, accessed: 1 June 2023., available at link: https://www.hops.hr/page-file/WlPNnbrbHaU6eAlL08kIG3/prequalification-process/Testiranje_sposobnosti_regulacijskih_jedinica_za_izvo-enje_mFRR.pdf [7] *"Afrr & in optimisation mathematical description for publication 01.04.2022"*, accessed: 5 June 2023., available at link: https://www.entsoe.eu/network_codes/eb/picasso/

[8] *"PICASSO MARI Stakeholder Workshop"*, accessed: 5 June 2023., available at link: https://eepublicdownloads.azureedge.net/webinars/2021/MARI_PICASSO_Stakeholder_Workshop_20211202-final.pdf

[9] *"Terms and conditions for balancing service providers on the ELES balancing market"*, accessed: 7 June 2023., available at link: https://www.eles.si/en/business-user-news/ArticleID/15326/Terms-and-conditions-for-balancing-service-providers-on-the-ELES-balancing-market

[10] *"Prequalification Process for Balancing Service Providers (FCR, aFRR, mFRR) in Germany ("PQ conditions")"*, accessed: 8 June 2023., available at link: https://www.regelleistung.net/Portals/1/downloads/regelenergieanbieter_werden/pr%C3%A4qualifikationsbedingungen/PQ Bedingungen - 03.06.2022 (englisch).pdf?ver=dXs9wAY6IAutEYL6PH7BTA%3d%3d

Petra Sagrestano Štambuk, Dajana Vrbičić Tenđera, Nikolina Zovko, Tomislav Tenđera and Marin Uzelac, Alignment of aFRR and mFRR prequalification process in Croatia with the target market design, Journal of Energy, vol. 72 Number 3 (2023), 3–7
https://doi.org/10.37798/2023723472

Journal of Energy

VOLUME 72 Number 3 | 2023

journal homepage: http://journalofenergy.com/

Optimizing Remaining Useful Life Estimation of Lithium-Ion Batteries: A Particle Swarm Optimization-Based Grey Prediction Model

Ali M Abdulshahed, Ibrahim Badi

***Summary* — Accurately estimating of the age and condition of lithium-ion batteries (LIBs) is paramount for their safe and economically viable utilization. However, assessing the degradation of these power units proves to be challenging due to their dependence on various environmental and usage factors. In this study, we propose an efficient Particle Swarm Optimization (PSO)-based Grey Theory prediction model to determine the Remaining Useful Life (RUL) of lithium-ion batteries. The proposed model utilizes PSO to optimize the coefficients of a grey prediction model, enabling accurate forecasting of the remaining useful life of LIBs. Our results demonstrate that the presented model outperforms conventional grey prediction models in terms of both accuracy and stability. Furthermore, the proposed model offers simpler predictions compared to existing models in the literature. By introducing this promising technique, our study contributes to the precise forecasting of the RUL of lithium-ion batteries and holds potential for applications in similar domains. This research serves as a significant step towards ensuring effective management and utilization of LIBs, promoting their reliability and safety.**

***Keywords* — Particle Swarm Optimization, Lithium-ion batteries, grey model**

I Introduction

The scarcity of fossil-fuel reserves, combined with the challenges of climate change, provides a significant motivation for the development of environmentally friendly transportation systems, sustainable energy sources, and intelligent grid networks. Successful implementation of these sectors necessitates the use of energy storage systems, which has garnered notable attention from researchers in recent times. In those fields, lithium-ion batteries are widely used. They play a significant role as one of the most important components and should be closely observed and managed. To ensure the economic feasibility of electric vehicles and the infrastructure of renewable energy systems and intelligent grids, it is imperative to have extended battery lifetimes. One of the most pressing and difficult issues is battery degradation during operation, which has become a limiting factor in a battery's lifetime. Lithium-ion batteries have become a extensively used technology due to their efficiency in storing and providing energy [4] LIBs are a class of rechargeable battery that has become well-known in recent years, because of their extended lifespan, impressive energy density and minimal self-discharge rate. Lithium-ion batteries find widespread use across various applications, including electric vehicles, consumer electronics, and stationary storage systems [2]. The high-energy density of lithium-ion batteries (LIBs) is a key advantage, as it allows for the storage of a larger quantity of energy inside a small form factor, compared to alternative rechargeable battery technologies. This attribute renders LIBs highly suitable for applications with limited space, such as mobile phones and laptop computers. In addition, lithium-ion batteries demonstrate a prolonged cycle life, indicating their ability to withstand numerous charge and discharge cycles without substantial capacity deterioration. This characteristic guarantees the ability of LIBs to undergoing repeated charging and discharging cycles, thus offering extended operational capabilities and durability. [20]. RUL is a substantial concept in the realm of lithium-ion battery technology. The term " RUL " could also be defined as the amount of time a battery can be used before it needs to be replaced [20].

Model-based methods involve the utilization of mathematical models, a collection of algebraic and empirical equations, and related parameters, which require experimentation and the analysis of large datasets [1]. Model-based approaches can construct the degradation behaviour of a battery, with either physics or regression models being employed. This extrapolation can predict battery performance. Recent research has demonstrated that physics models are more accurate for long-term predictions compared to empirical models, which often result in high errors [22].

The physics-based model for Remaining Useful Performance (RUP) [15], and RUL is predicted by integrating theories concerning reaction kinetics and electrode porosity. These theories are grounded in the physical and electrochemical processes occurring within the battery [1]. This type of model, also known as a white-box model, is a mathematical modelling technique that utilizes differential equations to mimic the behaviour of the system under consideration. These models are often able to be interpretable making them a popular choice for academic research. However, the physics-based model for RUL prediction has several drawbacks, including the need for specialized knowledge, difficulty in determining or recognizing model parameters, and high computational costs. [9]. Furthermore, measuring internal impedance at low frequencies is time-consuming and difficult. Another significant issue is that noises produced by other combined components of an online system affect the accuracy of electrochemical impedance spectroscopy (EIS) measurements as a result of the low-amplitu-

(Corresponding author: Ali M Abdulshahed)

Ali M Abdulshahed is with the Misurata University, Electrical and Electronic Engineering Department, Misurata, Libya (e-mail: a.abdulshahed@eng.misuratau.edu.ly)

Ibrahim Badi is with the Libyan Academy, Misurata, Libya (e-mail: i.badi@lam.edu.ly)

Ali M Abdulshahed, Ibrahim Badi, Optimizing Remaining Useful Life Estimation of Lithium-Ion Batteries: A Particle Swarm Optimization-Based Grey Prediction Model, Journal of Energy, vol. 72 Number 3 (2023), 8–13
https://doi.org/10.37798/2023723494

de signal required for EIS measurements. To address these issues, many researches advocate prediction based on empirical regression models [8], [14].

Data-driven models are a type of behavioural model that uses historical information to estimate the future behaviour within a system, specifically used here the Remaining Useful Life (RUL) of a battery. [1]. These models are based on the premise that past performance is indicative of future performance. In opposition to models based on physical equations, empirical models are founded on experimental data that can demonstrate the connections between inputs and outputs. Empirical-driven RUL prediction techniques can be classified under two groups: statistical modelling methods, such as regression paradigm, linear polynomial paradigm, and other parametric paradigms; non-parametric techniques, such as fuzzy logic systems (FLS), machine learning (ML), etc. [13]. Figure 1 Illustrates the key RUL forecasting methods for lithium-ion batteries [21].

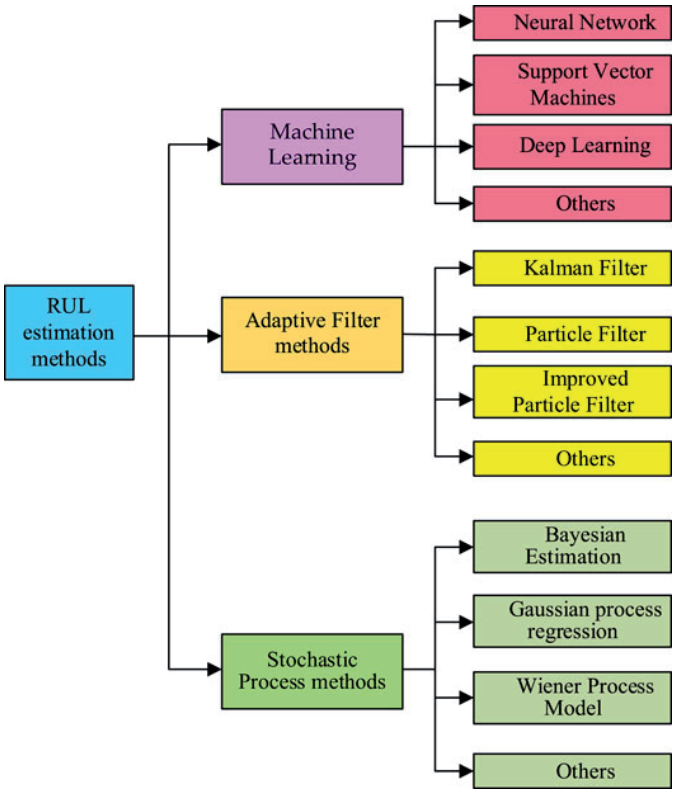

Fig. 1. Major RUL projection approaches [21].

Recently, the Deep Neural Network (DNN) has become a favourable technology for modelling a large volume of data [1]. This is due to its multilayer network structure, which allows for multiple activation or convolution operations within a single neuron, unlike the single activation function used in traditional Artificial Neural Networks (ANNs). This feature enables DNNs to be fed with data and extracts complex features and relationships from the data.

In [10] are introduced a deep neural network model combined with an exclusion layer to avoid data over-fitting, 11,345 data points were drawn from a single battery dataset for building a model. Nevertheless, the effectiveness metric the Root Mean Square Error (RMSE) was higher than expected at 3.427 due to limitations in hyperparameter tuning and insufficiently informative data for predictions. Despite these limitations, the underlying approach holds potential. Its ability to integrate an exclusion layer for preventing overfitting is a valuable innovation and could be further explored with a more comprehensive hyperparameter search and potentially richer or augmented datasets. Future research could investigate the impact of different network architectures or feature engineering techniques on model performance.

In a separate study [11] are introduced an enhanced Long Short-Term Memory (LSTM) method that was calibrated using Dataset collected from 28 batteries (NASA, Batteries No 5–7, Battery No 18, Batteries No 45–48, Batteries No 53–56, Batteries No 29–34, Battery No 36, Batteries No 38–44, Battery No 49, Battery No 51). The efficacy of the neural network was assessed with different battery discharge variables, and they found that RMSE decreases when the neural network is trained with more histories data. Although the proposed neural network was complex in nature, it could be reduced using more efficient optimization method and model selection. However, it may not be feasible to use these methods for forecasting Remaining Useful Life (RUL) in on-site engineering applications. In this context, while the enhanced LSTM method shows promise for battery RUL prediction, its complexity might make it less suitable for direct implementation in on-site engineering applications. Simpler models or cloud-based solutions might be more practical alternatives in such settings.

The work in [24] provides an in-depth look at the conducting of the optimized Grey model GM(1, 1) for estimating the RUL of lithium-ion batteries. The authors provide a comprehensive overview of the model and its implementation to battery life prognosis. They also discuss how the model can be used to optimize battery function and extend its life. The authors provide detailed analysis of their results, which demonstrate that the model is effective in predicting remaining useful life. Overall, this article provides a valuable resource for researchers interested in using this model for battery life prediction. To recap, the article's pros lie in its in-depth exploration of the GM(1,1) model, its practical implementation guidance, and its focus on optimizing battery life. This combination makes it a valuable resource for researchers and practitioners alike, contributing to the advancement of lithium-ion battery technology.

A solution is needed for situations where there is a limited amount of memory and computing power, which can use raw sensor data to calculate the state of health without requiring extensive preprocessing. The Grey model GM(1, N) (Tien, 2012) can be used as a modeling approach for prognosticating the Remaining Useful Life (RUL) of a lithium-ion battery. However, due to the non-linearity of the problem, traditional calibration methods such as the least square method may not provide an optimal solution. To address this issue, this work proposes a meta-heuristic method based on the behavior of natural swarms, namely the particle swarm optimization algorithm [7], to calibrate the GMC(1, N) coefficients [19]. This approach involves including a convolution integral in order to correct the modeling values by GMC(1, N) model. The proposed model is then used to prognosticate RUL of a lithium-ion battery.

In the area of battery health diagnostics, the Particle Swarm Optimization (PSO)-based Grey Prediction Model could presents a compelling alternative to data-hungry deep learning approaches. Its core strength lies in marrying the simplicity and interpretability of Grey models with the accuracy-enhancing power of PSO. This could lead to a model particularly well-suited for resource-constrained scenarios, where limited data or computational power restricts the deployment of complex deep learning architectures.

II. Methodology

A. *Grey modelling*

The Grey System approach, first founded in [5], [6], is a method dedicated to resolving problems with small sample sizes and incomplete information. This method can be utilized to analyse and evaluate vague systems when a certain component of knowledge is available. It generates, excavates, and extracts beneficial information from accessible data to accurately map out system behaviours as well as their implicit laws of development. The GM (1, N) model is one of the most extensively utilized in the recent literature in

Ali M Abdulshahed, Ibrahim Badi, Optimizing Remaining Useful Life Estimation of Lithium-Ion Batteries: A Particle Swarm Optimization-Based Grey Prediction Model, Journal of Energy, vol. 72 Number 3 (2023), 8–13
https://doi.org/10.37798/2023723494

order to express difficult behaviour through the use of a Black-Grey-White approach [19]. This methodology offers a broad and dynamic investigation on the relationship between parameters of a system. The term Accumulated Generating Operation (AGO) is a key aspect of Grey system theory, which can increase linearity and reduce randomness in samples. The primary chart of grey forecasting models presented in Figure 2 . In [18] and [19] are presented an enhanced Grey model based on the above-mentioned GM(1, N) model, whereby modelling values are improved by including a convolution integral GMC (1, N).

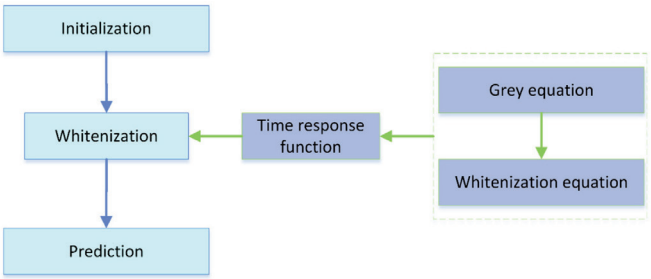

Fig. 2. Fundamental illustration of grey prediction frameworks [23].

The Grey theory models have conventionally been calibrated using the conventional least square's approaches. However, since the problem is nonlinear in nature, a strictly least square's solution may not suffice to adequately address this issue. To avoid the very long trial-and-error process, PSO can be utilized to enhance the Grey models' performance. The following section will review PSO and then describe the GMC (1, N) learning algorithm's main steps when used in conjunction with PSO.

Training GMC (1, N) by PSO

In [7] are proposed Particle Swarm Optimization (PSO) as a different evolutionary technique to existing algorithms. PSO draws upon the behaviour of real swarms, such as fish schools and bird flocks, and utilizes simple structures with a clear physical meaning for its optimization methodology. The algorithm forms a population of individuals-known as particles-where each behaves like an individual solution to the model, represented in an N-dimensional space. Each particle adjusts its location within this space using its own experience and the experience of its neighbours with regard to their current positions, velocities, and best previous positions. Unlike traditional algorithms that require the objective function to be differentiable, PSO is not constrained by such assumptions about the problem being solved. This makes it uniquely suitable for optimizing Grey model parameters without relying on the standard algorithms.

In this part, the primary steps of GMC(1, N) are depicted and its optimization procedure using PSO discussed. As GMC(1, N) aims to show the long-term behaviour of data and minimize the effect of random occurrences by conducting the AGO on the raw data, the first operation for building GMC(1, N) is to applying the initial Accumulated Generating Operation to the raw data. To calibrate the GMC(1, N) model, a suitable optimization technique such as PSO algorithm is employed for its potential to enhance complex numerical functions. Subsequently, an Inverse Accumulated Generating Operation (IAGO) is employed for the prediction of Remaining Useful Life (RUL). Figure 2 displays a schematic diagram of PSO-based Grey model detailing its modelling process. The modelling process is outlined in the following section:

Step #1: Examine the raw RUL data series as:

$$X_1^{(0)} = \left\{x_1^{(0)}(1+r),\ x_1^{(0)}(2+r), \dots, x_1^{(0)}(n+r)\right\}, \text{and}$$

$$X_j^{(0)} = \left\{x_j^{(0)}(1), x_j^{(0)}(2), \dots, x_j^{(0)}(p), \dots, x_j^{(0)}(p+n)\right\},$$

where j = 2,3,... N, s is the delay period of the system, the raw RUL data series has a length of p, while the number of values to be estimated is indicated by n.

Step #2: The 1st-order AGO sequences were obtained by processing the raw data of each variable (i.e., time series) using 1-AGO as follows:

$$X_1^{(1)} = \left\{x_1^{(1)}(1+r), x_1^{(1)}(2+r), \dots, x_1^{(1)}(p+s)\right\}, \text{and}$$

$$X_j^{(1)} = \left\{x_j^{(1)}(1), x_j^{(1)}(2), \dots, x_j^{(1)}(p), \dots, x_j^{(1)}(p+n)\right\},$$

$$\text{where } X^{(1)} = \sum_{i=1}^{K} x^{(0)}(i),\ K = 1,2,\dots,p+n.$$

Ref. [19] provides an in-depth overview of GMC(1,N), however this work will only include the core equations.

$$\frac{dX_1^{(1)}(K+r)}{dt} + a_1 X_1^{(1)}(K+r) = a_2 X_2^{(1)}(K) + a_3 X_3^{(1)}(K) + \cdots + a_N X_N^{(1)}(K) + u, \quad (1)$$

where K=1,2,…,p + n, the development coefficient is a_j, (j=2, 3,... N) , the driving coefficient is , and is the control parameter of a Grey model, respectively. Consequently, the output values can be given as:

$$\hat{X}_1^{(1)}(K+s) = x_1^{(0)}(1+s)e^{-a_1(K-1)} + \frac{1}{2} \times e^{-a_1(K-1)} \times f(1) + \sum_{\tau=2}^{K-1}\left[e^{-a_1(K-\tau)} \times f(\tau)\right] + \frac{1}{2} \times f(\tau) \quad (2)$$

where $f(\tau) = \sum_{i=2}^{N} a_i X_i^{(1)}(\tau) + u.$

To compute the parameters a_i, a_j and , the PSO algorithm could be applied to optimize the mathematical expression in Equation (2). The model is then calibrated until a desirable level of performance is achieved. The final optimal parameters are used in the GMC(1, 1) model in order to predict the RUL value. The following is a summary of the GMC(1, N) calibration process:

A particle in the PSO algorithm is parameters in the model that shifts its location from one iteration to the next based on velocity equation. Generally, if the space of search is D-dimensional, then the present velocity and position of the jth particle can be denoted by $A_j=[a_{j1}, a_{j2}, ..., a_{jD}]^T$ and $V_j = [v_{j1}, v_{j2},..., v_{jD}]^{\wedge}T$ respectively.

where j = 1, 2, ... M and M is the particles number of the swarm.

Particle j is able to recall the best location it has achieved so far, referred to as the best position locally $[Pbest_j = [pbest_1, pbest_2,..., pbest_{jD}]^T$. Moreover, it can also move to the best position that the whole swarm has obtained, known as the best position globally $[Gbest_j = [gbest_1, gbest_2,..., gbest_{jD}]^T$. To start with, particle j's initial velocity and position are determined randomly. Subsequently, particle j changes its velocity for iteration $k+1$ based on the best positions (i.e. locally and globally) in addition to its velocity from iteration k with this Equation (3):

$$V_j(k+1) = \omega V_j(k) + c_1 R\left(Pbest_j(k) - B_j(k)\right) + c_2 R\left(Gbest_j(k) - B_j(k)\right) \quad (3)$$

Where, ω is the inertia factor, which is conducted to regulate the effect of the previous velocities on the present velocity. The term c1 is the self-confidence, and the term c2 is the swarm-confidence factors. R is a random number that can change from 0 to 1. The position of particle j in iteration k+1 can be computed using the improved velocity as follows:

$$A_j(k+1) = A_j(k) + V_j(k+1) \quad (4)$$

The value of a particle is determined by an objective function that computes the difference between the particle and its optimum solution, as follows:

Ali M Abdulshahed, Ibrahim Badi, Optimizing Remaining Useful Life Estimation of Lithium-Ion Batteries: A Particle Swarm Optimization-Based Grey Prediction Model, Journal of Energy, vol. 72 Number 3 (2023), 8–13
https://doi.org/10.37798/2023723494

$$f(A_j) = \sum_{k=1}^{N} [\hat{x}^{(0)}(k) - x^{(0)}(k)],^2 \quad (5)$$

The fitness value, $f(A_j)$, is calculated by comparing the target output $\hat{x}^{(0)}(k)$ to the predicted output $x^{(0)}(k)$ based on the updating of the particles (i.e., solutions).

Step #3: In a new iteration compute the new particle velocity and particle position using formula in Equations (3) and (4), respectively, then update the model variables in Equation (2).

Step #4: If the value of error is within the model's requirements or a set number of epochs have been completed, the calibration of the model will be finished. If not, it will go back to Step #3.

Step #5: Set the best parameters B_j.

Step #6: 1- IAGO can be utilized to acquire the anticipated values. The mathematical equation is as follows:

$$\hat{x}_1^{(0)}(K+r) = \hat{x}_1^{(1)}(K+r) - \hat{x}_1^{(1)}(K-1+r), \text{ and } \hat{x}_1^{(0)}(1+r) = \hat{x}_1^{(1)}(1+r). \quad (6)$$

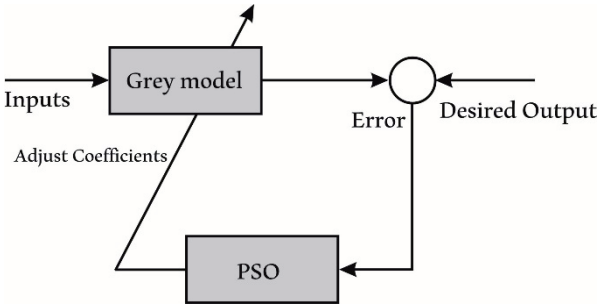

Fig. 3. Illustrative diagram of GMCPSO(1, 1) model.

III. Experimental Work

The diminishment of a battery's effectiveness is associated with multiple processes, and its decline follows a nonlinear manner. Consequently, battery aging data must be acquired to develop an RUL prediction model and consider its accuracy and robustness. The Prognostics Centre of Excellence at NASA Ames provides a widely-utilized battery dataset [17]. This dataset includes four types of batteries packs (#5, #6, #7, and #18). Figure 3 illustrates the decrease in battery capacity that is present in the dataset.

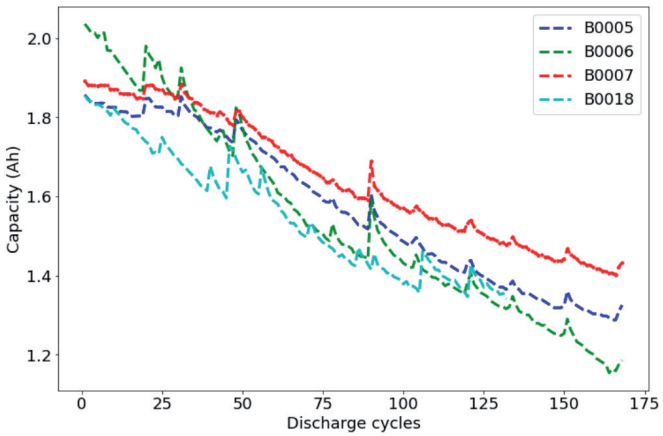

Fig. 4. Battery capacity decay trend that is present in the dataset.

The principle of Constant Current Constant Voltage (CC-CV) is a frequently employed technique for battery charging. In this process, the current is first kept at a constant level of 1.5 A until the voltage reaches a limit of 4.2 V. After this, the voltage remains fixed while the current gradually decreases to 20 mA, thus completing the CC-CV charging process (see Figure 4). For discharging, four batteries are typically discharged at a constant current of 2 A until their respective voltages reduce to 2.7 V, 2.5 V, 2.2 V, and 2.5 V respectively.

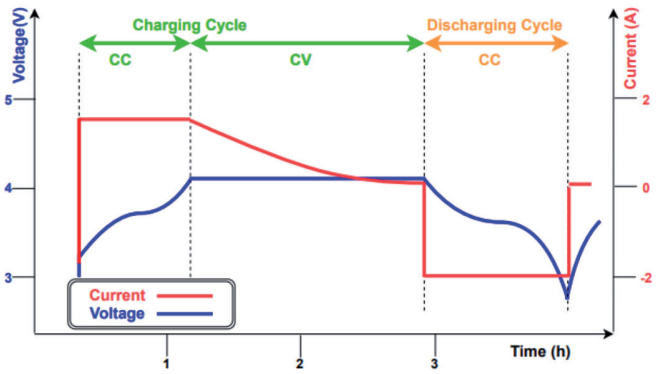

Fig. 5. illustrates the Constant Current-Constant Voltage process used in the NASA dataset [16].

The experiment persisted until the measured actual capacity of each battery fell below 70% of its rated 2Ah. This Aging Point Threshold (APT) denoted a substantial decline in performance, signifying the point at which further exploration yielded diminishing returns. These data points are well-established in the scientific community and have been actively incorporated in current studies [3], [12].

A. Main Steps in GMC(1,1) Modelling

Input for GM(1,1) Time Series Model:

– Time Series Data: The primary input for the GMC(1,1) model is a univariate time series dataset.

– This dataset typically includes a sequence of observations recorded over equally spaced time intervals.

Data Preprocessing:

– Ensure that the time series data is in a suitable format for analysis.

– Handle any missing values or outliers in the data.

Grey System Modeling:

– Original Data Sequence: Transform the original time series data into a first-order accumulated series.

– Establishment of Grey Differential Equation (GDE): Develop a differential equation based on the accumulated series.

– Parameter Estimation: Estimate the model parameters, which include the development coefficient and the grey input coefficient.

GM(1,1) Model Solution:

– Solve the established grey differential equation to obtain the predicted values of the original time series.

Model Evaluation:

– Assess the performance of the GMC(1,1) model using

Ali M Abdulshahed, Ibrahim Badi, Optimizing Remaining Useful Life Estimation of Lithium-Ion Batteries: A Particle Swarm Optimization-Based Grey Prediction Model, Journal of Energy, vol. 72 Number 3 (2023), 8–13
https://doi.org/10.37798/2023723494

appropriate metrics.

Compare the predicted values with the actual values to validate the model's accuracy.

B. Results

To optimize the GMC(1, N) coefficients, the historical dataset was split into two separate sets: one for computing the model (around 48%) and the other for testing purposes (around 52%). The Python environment was utilized for the creation and simulation of the RUL model. The designed model was organized as outlined below:

Step #1: the mathematical operation (1-AGO) is used to enhance the linearity of the raw data and minimize any randomness present in the measured samples.

Step #2: the optimization algorithm PSO is used to train the GMC(1, N) model, as was mentioned in the previous section.

Step #3: The RUL value is calculated by performing an IAGO (Inverse Accumulated Generating Operation).

For the PSO algorithm, 70 particles were used with self-confidence factor C_1 set to 1.4 and swarm-confidence factor C_2 set to 1.4. The inertia weight ω was adapted over 150 epochs, decreasing from 0.8 to 0.2. At the end of this process, the total error was satisfactory (RMSE=1.03).

In this section, the development of another separate Grey model was conducted using the conventional Least Squares (LS) method. Three steps were involved throughout this process, with Steps 1, 2, and 3 being similar to those presented in the above mention's section. The Grey variables of Equation 2 were then determined by applying the traditional least squares method.

After training a model, it becomes essential to validate the model to evaluate its prediction quality and the accuracy of its parameters. This will provide the designer with confidence in the model and indicate whether any revisions to the training process are necessary. Model validation is a procedure that involves several steps. The exhibitions of the frameworks utilized in this exploration were determined using Mean Absolute Percentage Error (MAPE) as follows:

$$MAPE = \frac{1}{n}\sum_{i=1}^{n}\frac{\left|mes_k - pre_k\right|}{mes_k}$$

where,

mes_k: Measured RUL;
pre_k: Predicted RUL;
$\overline{mes}$, $\overline{pre}$: Average of the measured value and predicted value, respectively; and
n: The number of measured data.

In this section, the optimization process was applied to the final Grey theory models. Following this, a previously unused testing dataset was utilized to evaluate the performance of the models, which had not been used during the optimization stage. The outcomes acquired for the GMCPSO(1,1) model and GMC(1,1) model are exhibited in Figure 4 and Figure 5, correspondingly.

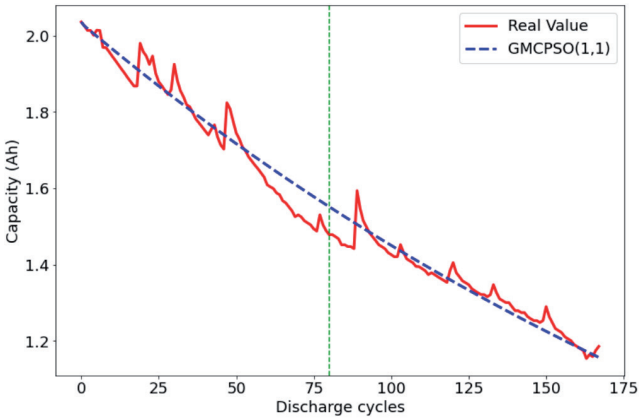

Fig. 6. RUL prediction using GMCPSO(1, 1) model.

The red-solid line indicates the capacity degeneration process, while the blue dash line denotes the predicted capacity by GMCPSO(1, 1) model. The final Grey model parameters obtained are listed in Table 1:

Table 1

The final Grey model parameters for GMCPSO(1, 1) model.

a_1	a_2	MAPE
0.00337	0.00337	0.019

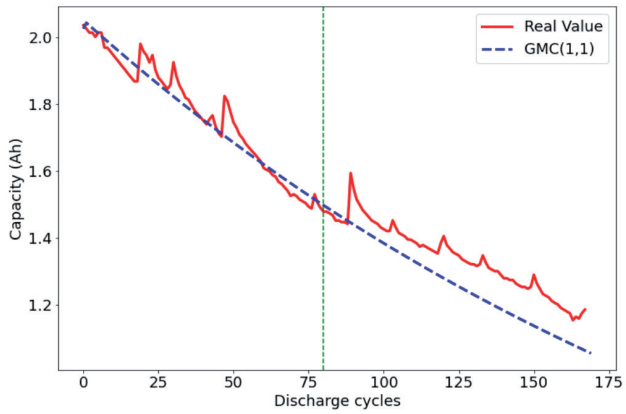

Fig. 7. RUL prediction using GMC(1, 1) model

The red-solid line indicates the capacity degeneration process, while the blue dash line denotes the predicted capacity by GMC(1, 1) model. The final Grey model parameters obtained are listed in Table 2:

Table II

The final Grey model parameters for GMC(1, 1) model.

a_1	a_2	MAPE
0.00393	522.565	0.03811

The results of this study reveal that the Mean Squared Prediction Error (MSPE) for the PSOGMC(1,1) model was 0.019, while the MSPE for the GMC(1, 1) model was 0.03811. This implies that the proposed PSOGMC(1,1) model is more precise than the GMC(1, 1) model in predicting RUL. This is due to the fact that the PSOGMC(1,1) model utilizes PSO for the optimization of GMC(1, 1) model parameters. The PSO algorithm is an iterative optimization method that uses a population of particles to search for optimal solutions. By using this approach, the PSOGMC(1, 1) model can find better solutions than those found by traditional methods such as

Ali M Abdulshahed, Ibrahim Badi, Optimizing Remaining Useful Life Estimation of Lithium-Ion Batteries: A Particle Swarm Optimization-Based Grey Prediction Model, Journal of Energy, vol. 72 Number 3 (2023), 8–13
https://doi.org/10.37798/2023723494

LS algorithms. Additionally, it was found that the true Remaining Useful Life (RUL) of the battery was 84 charge-discharge cycles in total. The RUL prediction results achieved by GMC(1, 1) and PSO-GMC(1,1) models were 119 and 87 respectively; demonstrating that PSOGMC(1,1) model performed better than GMC(1, 1).

This study employs a Particle Swarm Optimization (PSO)-based Grey Prediction Model. This approach offers potential advantages:

Simplicity: Grey models are generally simpler to construct and implement compared to complex deep learning models [3].

Limited Data: Grey models can often perform well with limited data, which can be advantageous in situations where large datasets are unavailable.

Optimization: The use of PSO to optimize the grey model's coefficients may enhance its accuracy.

Grey theory modeling is a powerful tool for predicting the RUL of lithium-ion batteries. This approach can be employed to gauge the RUL of a battery based on its current usage and state patterns. Once a prediction of the RUL has been calculated, it can be used to take decisions about when to replace a battery. For instance, if a battery has an estimated RUL of two years but is only being used once per week, then it may not need to be replaced until after 3 years have passed. On the other hand, if a battery has an estimated RUL of one year but is being used multiple times per day, then it may need to be exchanged sooner than anticipated in order to ensure optimal functioning. However, like any approach, it also has its limitations. One limitation of this approach is the reliance on optimization techniques such as PSO. While PSO can effectively optimize the coefficients of the grey prediction model, it may require significant computational resources and time to find the optimal solution. This can be a drawback in real-time or time-sensitive applications where quick predictions of RUL are required.

IV. Conclusions

This study presents a novel grey modelling methodology with the objective of effectively forecasting the Remaining Useful Life (RUL) of lithium-ion batteries (LIBs). The evaluation of the proposed methodology is conducted utilizing the dataset on battery charge-discharge cycles provided by NASA. The findings indicate that the RUL prediction model possesses the capability to significantly enhance the dependability and security of energy storage systems.

The grey theory modelling approach combines grey system theory and optimization techniques to model the battery's historical data and extract valuable information for predicting its RUL. The proposed modelling method is carefully compared with existing Grey modelling methods in terms of accuracy and computational efficiency. The experimental findings demonstrate that the suggested approach outperforms the current model in both output accuracy and computational efficiency.

Furthermore, this paper provides insights into how to further improve the accuracy of RUL prediction by incorporating additional factors such as current, voltage, temperature, etc., into the model. Further research and development are necessary to address above mentioned limitations and enhance the accuracy and reliability of RUL estimation for practical applications.

Acknowledgment

We are grateful to all those who provided their support and expertise in the creation of this article, without any financial assistance.

References

[1] S. Ansari, A. Ayob, M.H. Lipu, A. Hussain, and M.H.M. Saad. Remaining useful life prediction for lithium-ion battery storage system: A comprehensive review of methods, key factors, issues and future outlook, *Energy Reports*, vol. 8, pp. 12153-12185. 2022.

[2] S. Bockrath, V. Lorentz, and M.Pruckner. State of health estimation of lithium-ion batteries with a temporal convolutional neural network using partial load profiles, *Applied Energy*, vol. 329, 120307, 2023.

[3] C. Chen, J. Wei, and Z. Li. Remaining useful life prediction for lithium-ion batteries based on a hybrid deep learning model. *J Processes*, vol. 11, no. 8, 2333, 2023.

[4] Y. Chen, Y. Kang, Y. Zhao, L. Wang, J. Liu, Y. Li, Z. Liang, X. He, X. Li, N. Tavajohi, and B. Li. A review of lithium-ion battery safety concerns: The issues, strategies, and testing standards, *Journal of Energy Chemistry*, vol. 59, pp. 83-99, 2021.

[5] J.-L. Deng. Control problems of grey systems, *Systems & Control Letters*, vol. 1, no. 5, pp. 288-294, 1982.

[6] J.-L. Deng. Introduction to grey system theory, *The Journal of grey system*, vol. 1, no. 1, pp. 1-24, 1989.

[7] R.C. Eberhart, and J. Kennedy. *A new optimizer using particle swarm theory.* Proceedings of the sixth international symposium on micro machine and human science (MHS'95), Nagoya, Japan, 1995.

[8] W. He, N. Williard, M. Osterman, and M. Pecht. Prognostics of lithium-ion batteries based on Dempster–Shafer theory and the Bayesian Monte Carlo method, *Journal of power sources*, vol. 196, no. 23, pp. 10314-10321. 2011.

[9] X. Hu, L. Xu, X. Lin, and M. Pecht. Battery lifetime prognostics. *Joule*, vol. 4, no. 2, pp. 310-346, 2020.

[10] P. Khumprom, and N. Yodo. A data-driven predictive prognostic model for lithium-ion batteries based on a deep learning algorithm, *Energies*, vol. 12, no. 4, 660, 2019.

[11] Li, P., Zhang, Z., Xiong, Q., Ding, B., Hou, J., Luo, D., . . . Li, S. (2020). State-of-health estimation and remaining useful life prediction for the lithium-ion battery based on a variant long short term memory neural network. *Journal of power sources, 459*, 228069.

[12] Z. Li, F. Bai, H. Zuo, and Y. Zhang. Remaining Useful Life Prediction for Lithium-Ion Batteries Based on Iterative Transfer Learning and Mogrifier LSTM, *J Batteries*, vol. 9, no. 9, 448, 2023.

[13] M.H. Lipu, M. Hannan, A. Hussain, M. Hoque, P.J. Ker, M.M. Saad, and A. Ayob. A review of state of health and remaining useful life estimation methods for lithium-ion battery in electric vehicles: Challenges and recommendations, *Journal of cleaner production*, vol. 205, pp. 115-133, 2018.

[14] M.V. Micea, L. Ungurean, G.N. Cârstoiu, and V. Groza. Online state-of-health assessment for battery management systems, *IEEE Transactions on Instrumentation Measurement*, vol. 60, no. 6, pp. 1997-2006, 2011.

[15] B. Pattipati, C. Sankavaram, and K. Pattipati. System identification and estimation framework for pivotal automotive battery management system characteristics, *IEEE Transactions on Systems, Man, Cybernetics, Part C*, vol. 41, no. 6, pp. 869-884, 2011.

[16] T. Pham, L. Truong, H. Bui, T. Tran, A. Garg, L. Gao, and T. Quan. Towards Channel-Wise Bidirectional Representation Learning with Fixed-Point Positional Encoding for SoH Estimation of Lithium-Ion Battery, *Electronics*, vol. 12, no. 1, 98, 2023.

[17] A. Saxena, J.R. Celaya, I. Roychoudhury, S. Saha, B. Saha, and K. Goebel. *Designing data-driven battery prognostic approaches for variable loading profiles: Some lessons learned*, European conference of prognostics and health management society, Dresden, Germany, 2012.

[18] T.-L. Tien. The indirect measurement of tensile strength of material by the grey prediction model GMC (1, n), *Measurement Science and Technology*, vol. 16, no. 6, pp. 1322-1328, 2005.

[19] T.-L. Tien. A research on the grey prediction model GM (1, n). *Applied Mathematics and Computation*, vol. 218, no. 9, pp. 4903-4916, 2012.

[20] F.-K. Wang, Z.E. Amogne, J.-H. Chou, and C. Tseng. Online remaining useful life prediction of lithium-ion batteries using bidirectional long short-term memory with attention mechanism, *Energy Reports,* vol. 254, Part B, 124344, 2022.

[21] S. Wang, S. Jin, D. Deng, and C. Fernandez. A critical review of online battery remaining useful lifetime prediction methods, *J Frontiers in Mechanical Engineering*, vol. 7, 719718, 2021.

[22] Y. Xing, E.W. Ma, K.-L. Tsui, and M. Pecht. An ensemble model for predicting the remaining useful performance of lithium-ion batteries, *Microelectronics Reliability*, vol. 53, no. 6, pp. 811-820, 2013.

[23] N. Xu, Y. Dang, and Y. Gong. Novel grey prediction model with nonlinear optimized time response method for forecasting of electricity consumption in China, *Energy Reports*, vol. 118, pp. 473-480, 2017.

[24] D. Zhou, L. Xue, Y. Song, and J. Chen. On-line remaining useful life prediction of lithium-ion batteries based on the optimized gray model GM (1, 1), *Batteries*, vol. 3, no. 3, 21, 2017.

Journal of Energy

VOLUME 72 Number 3 | 2023

journal homepage: http://journalofenergy.com/

Development of transformers with natural ester and cellulose or aramid insulation

Ramazan Altay, İrem Hazar, Mahmut Aksoy, Hakan Aktay, Jean-Claude Duart, Radoslaw Szewczyk

***Summary* — This study describes selected research studies performed for developing design rules for power transformers using natural esters. The presented simulation results verified adequacy of design rules and allowed for adjustments needed for implementing the new insulation system vs. the one based on mineral oil and cellulose-based solid insulation. They were also used as a base for the next transformer design combining natural ester with aramid insulation.**

***Keywords* — Natural ester liquid, electric field distribution, computational fluid dynamics, aramid insulation**

I. Introduction

Modernization of distribution networks increasingly uses transformers utilizing advanced insulation systems based on solid and fluids that have been developed in the recent decades. Taking into accounts new usages of energy, whether they are related to the need for charging electrical vehicles, the integration of renewable energy (wind, solar) or the increase of population in cities leading to higher power demand, it is a constrain that leads to higher stress for electrical equipment like transformers or cables. The manufacturers of such equipment have then to consider evolution of the designs and may need to adopt new materials. Amongst those new materials we can mention about the new generation of core steel with low losses but also new insulation materials that will tend to replace the historical materials being used. This is particularly true in liquid filled transformers where cellulose paper and pressboard combined with mineral oil have been the most common materials used for several decades. The advanced material solutions offer extended lifetime to the insulation system, increased overloadability for the transformers, increased power density, as well as equipment compactness and higher fire resistance or improved sustainability. The last item is mainly related to the usage of natural ester that lowers the carbon footprint as it is biodegradable.

For the solid insulation the most used material is produced in a paper and a pressboard form but made of synthetic fibers. Those fibers were invented in the late 1950's and result from an improvement of the known nylon chemistry. However, a modification of the nylon molecule with addition of aromatic rings led to the invention of aromatic polyamides, known as aramid fibers. Typical historical applications of aramid-based insulation in liquid filled transformers include on-board traction transformers, wind turbine step-up transformers and transportable mobile transformers for emergency or temporary use. In recent years, aramid insulation has been successfully evaluated and implemented at several distribution system operators (DSOs) in transformers utilizing sustainable peak loading concept or when looking for more grid resiliency [1].

It is also important before looking into a new application to consider design simulations that will help to assess such materials. Some extended work needs to be conducted to understand applicability of the advanced design in such new applications. For example, in wind turbine applications for offshore installations the benefit that advanced materials can have on the design can impact the overall design of the transformers but also the nacelle, where transformers are generally located.

Transformers for solar applications are different from regular transformers in two ways. They can be exposed to a considerable amount of harmonic content due to DC/AC conversion and a typical daily loading cycle that is dependent on the daily sunlight cycle. The daily sunlight can be typically described as a bell-curve as shown in Fig. 1. Both phenomena will have an impact on the temperature rise of the different transformer parts. Two tools have been developed to predict the impact of the harmonics and to take the cyclic daily load into account. A reference transformer of 1600 kVA was evaluated, and different insulation systems have been compared.

For larger power transformers the studies of the electrical field distribution as well as the impact on the cooling from those new materials are important and need to be studied. Adapted numerical model will help to assess the impact on operating temperature inside the transformer while external conditions like ambient temperature must be considered. A 70 MVA transformer design optimization integrating natural esters has been studied.

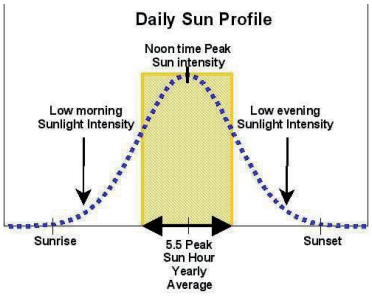

Fig. 1. Example of daily sun profile.

(Corresponding author: Ramazan Altay)

Ramazan Altay, İrem Hazar and Mahmut Aksoy are with the BEST Balikesir Elektromekanik Sanayi Tesisleri A.S., Balikesir, Turkey (e-mails: ramazan.altay@besttransformer.com, irem.hazar@besttransformer.com, irem.hazar@besttransformer.com)

Hakan Aktay is with the Opti-Consult, Konak/İzmir, Turkey (e-mail: hakan.aktay@opti-consult.org)

Jean-Claude Duart is with the DuPont Specialty Products Operations Sarl, Geneva, Switzerland (e-mail: JEAN-CLAUDE.DUART@dupont.com)

Radoslaw Szewczyk is with the DuPont Polska Sp. z o.o., Warsaw, Poland (e-mail: radoslaw.szewczyk@dupont.com)

https://doi.org/10.37798/2023723506

As a second step the design needs to be optimized and the construction parameters as well as the safety margins will need to be chosen for the windings to prepare pilot units to be produced. This is why a study on these construction elements has been carried out. Historical behavior of materials as well as thermal analysis must help to select the proper levels for designing the windings safely.

II. Insulation Systems for Distribution and Power Transformers

Distribution transformers have a general winding construction which differs from larger power transformers since they operate at lower voltages, generally below 36 kV. However, in recent years we have seen such construction styles to be used in transformers up to 66 kV, particularly in wind turbine transformers. Generally, a distribution winding style uses foil winding in the low voltage coil and layer winding with conductors, round or rectangular, in the high voltage coil as shown in Fig. 2.

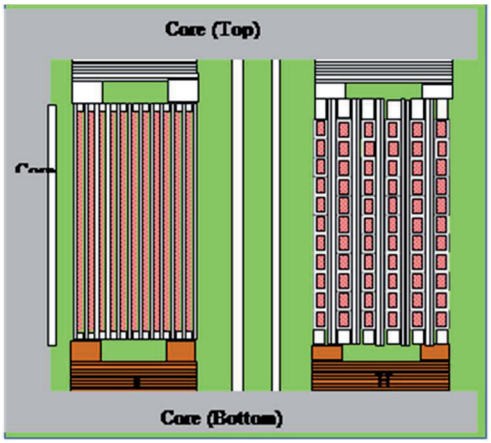

Fig. 2. Example of winding construction for distribution transformers with aramid-based insulation system.

Fig. 3 shows example constructions of various insulation systems for power transformers. Typical arrangement for LV and HV disc windings is shown with different extent of aramid insulation utilized in different winding constructions. In semi-hybrid system, only the conductor insulation uses aramid insulation paper. With this construction the impact of overheating of the windings leading to extensive gassing from the cellulose components in the winding area is limited as aramid degradation is not expected until copper reaches extreme temperatures. In hybrid system, the use of aramid extends from conductor insulation towards pressboard components in vicinity of conductor. But there are still cellulose-based materials used for other insulation components in the winding assembly. Those cellulose-based components together with overheated liquid could give DGA indications on thermal problems within the transformer.

The most insensitive insulation system to higher temperatures resulting from operation or from external factors (like higher power demand or higher ambient temperatures) would be full high temperature insulation systems or "hybrid plus" insulation systems where aramid insulation is combined with ester fluids. In these systems, the use of aramid is most extensive for different insulation parts, and the distance from hot conductors to cellulose components may be significant. In some cases, cellulose components would not be used in the transformer construction at all. In such cases, the liquid may be the only component generating gasses and data useful for conventional transformer diagnostics. However, some work to look for tracers from aramid thermal degradation has been engaged in recent years leading to better understanding of the ageing protocols [2].

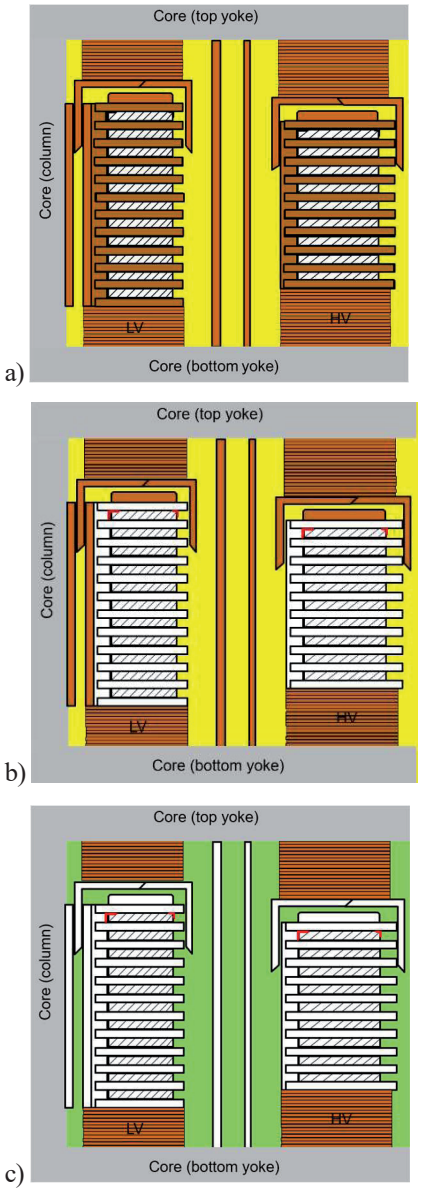

Fig. 3. Example constructions of various insulation systems with aramid: a) semi-hybrid, b) hybrid, c) "hybrid plus" with ester (white color indicates aramid insulation).

III. Simulation Studies of Various Transformer Designs

The use of advanced design tools has allowed optimization of the transformer design over the years. The work reported in this paper refers to two studies: the first one on a 1600 kVA unit for PV solar application, and the second study has been done on a power transformer 70 MVA integrating natural ester as a cooling and insulating fluid.

A. Simulation study of 1600 kVA solar power transformer

1. Influence of harmonics

The current generated by the PV panels is DC and in order to connect the solar plant output to the grid, the current has to be

Ramazan Altay, İrem Hazar, Mahmut Aksoy, Hakan Aktay, Jean-Claude Duart, Radoslaw Szewczyk, Development of transformers with natural ester and cellulose or aramid insulation, Journal of Energy, vol. 72 Number 3 (2023), 14–21
https://doi.org/10.37798/2023723506

inverted to AC. The inverted current is far from the ideal sinusoidal shape and thus contains a high level of harmonics. Most of the distribution companies have limits on the amount of harmonics one can connect to their grid (typical 5%, or in Europe even 2.5% total harmonic distortion, THD). One way or the other, the current must be filtered by harmonic filters and that can be done before or after transformation. In large solar power plants there are typically 2 transformations,

e.g. a 100 MVA plant could have 50 units of 2000 kVA going from 400 V to 20 kV and then 1 unit of 100 MVA from 20 kV to 110 kV (or higher). It is cheaper to opt for 1 harmonic filter before the 100 MVA transformer instead of installing 50 filters before each of the 2000 kVA transformers. Let us consider, for the case of argument, that the AC current entering the typical distribution transformer is not filtered. In that case, the transformer manufacturer needs to know the harmonic content of the current entering the transformer. There are 4 ways this information is given to the manufacturer:

1. The customer knows about harmonic problems and overrates the transformer and orders the transformer as such. (In other words, he knows the factor-K.)
2. The customer gives the THD or gives the value of each harmonic in %. In the first case the supplier shall have to convert the THD into a % for each harmonic.
3. The customer gives the K-factor (different from factor-K). The supplier shall then multiply the additional losses with this K-factor, in order to predict the real losses generated in the transformer.
4. The customer has never heard of harmonics. In that case, the manufacturer has to follow a guideline to assume a certain K-factor.

Typically, with no information the transformer should be calculated with a K-factor of 15 [3]. The relation between THD and K-factor will be explained later. To summarize, harmonic content can be translated in a K-factor. This factor is used to multiply the additional losses in the transformer, resulting in higher real load losses and thus resulting in higher temperatures.

2. K-factor/factor-K tool

A tool has been developed to calculate the K-factor and factor-K. It is important to understand the difference between the two factors. The K-factor is the factor the transformer manufacturer has to use to multiply the additional losses. That way the real losses and temperature can be estimated. The factor-K is a factor by which one can derate or upgrade a transformer to cope with the harmonic content or to give an equivalent sinusoidal rate. Table I provides an example of a harmonic spectrum till the 25th harmonic that will be used of the optimization of the 1600 kVA design (cellulose, mineral oil).

Table I

Percentual Part of Nth Harmonic in Nominal Current

harmonic	I h (%) I_n %I_{nom}
1	86.12693
3	36.58379
5	21.95027
7	15.67877
9	12.19460
11	9.97740
13	8.44241
15	7.31676
17	6.45596
19	5.77639
21	5.22626
23	4.77180
25	4.39005
Inom	100.0

Using industry experience [4] and the example of the harmonic spectrum, the tool allows to derive a THD value of 0.59 corresponding to the same harmonic content as indicated in the Table II.

Table II

Output Example of The Calculation Tool

thd	0.59		
alfa	thd/0.463		1.27429806
i1	(1/1+thd^2)^0.5	1	86.1269258
ix	alfaix/x	3	36.5837914
		5	21.9502748
		7	15.6787677
		9	12.1945971
		11	9.97739764
		13	8.44241339
		15	7.31675827
		17	6.45596318
		19	5.77638811
		21	5.22625591
		23	4.77179887
		25	4.39005496

Then the tool calculates the K-factor which is in this case 15.1962. For deriving the factor-K, we need transformer losses values as show in Table III.

Table Iii.
1600 KVA Transformer Losses

Calculated additional losses HV [W]	617
Calculated additional losses LV [W]	262
DC losses HV [W]	8280
DC losses LV [W]	5427
DC losses leads [W]	410
Additional losses outside windings [W]	318
Additional losses/ DC losses [%]	8.5

The resulting factor-K is then calculated together with the derating factor. Values are reported in Table IV.

Table IV

Derating Factor and Factor-K for 1600 KVA Transformer

Derating-factor with harmonic content	0.862
Factor-K to determine equivalent sinusoidal load	1.160

The interpretation of this information is the following: If the 1600 kVA transformer is loaded with this harmonic content

as described in the example, the transformer can be loaded with maximum 1380 kVA to avoid overheated and accelerated degradation of the insulation system based on cellulose. On the other hand, if the nameplate of the transformer indicates 1600 kVA with K-factor 15 explicitly mentioned, the transformer could be loaded with a sinusoidal load of 1856 kVA.

Ramazan Altay, İrem Hazar, Mahmut Aksoy, Hakan Aktay, Jean-Claude Duart, Radoslaw Szewczyk, Development of transformers with natural ester and cellulose or aramid insulation, Journal of Energy, vol. 72 Number 3 (2023), 14–21
https://doi.org/10.37798/2023723506

3. Influence of load cycles

It is trivial, that output of PV cells follows the cycle of the daylight. During the night we can assume that only no-load- losses will be present. During the day the output follows the cycle of the sun. This results in a bell-shape load profile. In the theoretical profile, and assuming a daily 12 h daylight, sigma of the bell curve is 2 h resulting in 68% of the daily energy being concentrated in a period of 4 h (the +/-3 sigma being the 12 h daylight is then theoretically 99.7% of the daylight). The load will result in losses that in their turn result in temperature variations. The goal of the study is to investigate whether it is possible to design an ideal cooling structure that can cope with those loads. Aging of insulation material and general safety limits must be evaluated and compared for different insulation/cooling systems. Intuitively we can already see that larger units (with important time-constants) could probably be overloaded. By the time the transformer reaches critical temperatures, the load is already going down. There are some guidelines to come up with dynamic temperature calculations. However, these analytical formulas are not sufficient to describe the models we are investigating. Therefore, a new calculation tool was created and will be describe further.

4. Load cycle tool

The model is based on a 4-body mass heat exchange. The original theoretical model was a 3-body mass heat exchange solved analytically [5]. In this study the model was expended to 4-body mass and the problem (system of four ordinary differential equations) was solved by the numerical method Runge-Kutta 4th order.

The four bodies in our system are: core, LV winding, HV winding and oil-tank while originally LV and HV windings were treated as one single body. The steady state temperature rises are considered for core, LV and HV, the rise over the average oil temperature. Specific heat for the different materials is filled in with the values from original model. In what follows, the specific heat for aramid and ester oil were kept with the same value as for cellulose and mineral oil. Load is then input in the calculation tool for the 1600 kVA, and it is assumed a cold start and a load of continuous 100%, which then results in the following temperature rises as shown in Fig. 4.

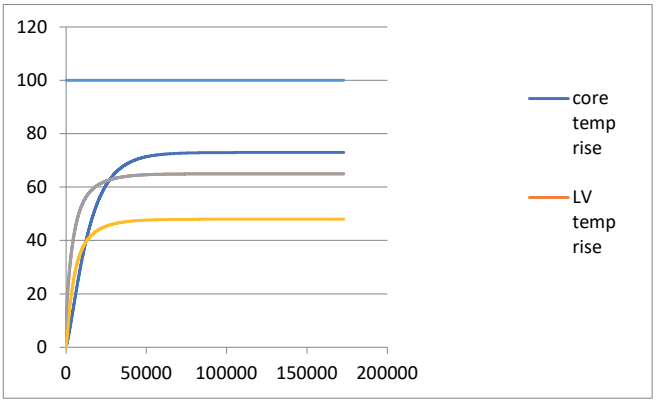

Fig. 4. Temperature rise for 1600 kVA transformer.

We can see that after around 50000 seconds (14 h) the transformer reaches steady state conditions. 73°C for core, 65°C for LV and HV, 48°C for average oil (48 / 0.8 = 60). This is trivial because our model is based on the calculated steady state values. All temperatures are temperature rises over ambient.

5. Evaluation of reference 1600 kVA transformer

As a first exercise we are going to evaluate what is happening with the temperatures with a typical loading cycle. Then we are going to look at what possibilities there are with regard to overload when we replace the insulation materials and the oil. We are assuming daylight between 7 AM and 7 PM, if we apply the Bell-curve model then we can generate a load profile with the equation (1):

$$load\ pu = \frac{1}{\sigma * \sqrt{2\pi}} * e^{\frac{-(x-\mu)^2}{2*\sigma^2}} \quad (1)$$

Where μ is the average time between 7 AM and 7 PM, 13.5 and σ is the standard deviation of 2 h. This gives a per unit graph were the total surface under the curve is 1. In order to translate this in % load we have to divide by the maximum value (at 13.5 h) and multiply by 100. For the reference transformer, this results in the following 2 days cycle as shown in Fig. 5, assuming cold start at midnight of the first day, and only no-load losses till 7 AM are show in Table V.

Table V

Calculated Values for Temperature Rises in 1600 KVA Transformer

	Core rise	LV rise	HV rise
	50.43386539	50.99716039	51.01126495
Gradient max	14.52883171	Average oil rise	36.48243324
Hot-spot rise	61.58475643	Top oil rise	45.60304155

In this case we see that the temperatures are far under what is allowed by standards (60/65/78°C) as we only reach 46/51/62°C for the top oil rise, average winding rise and hot spot rise.

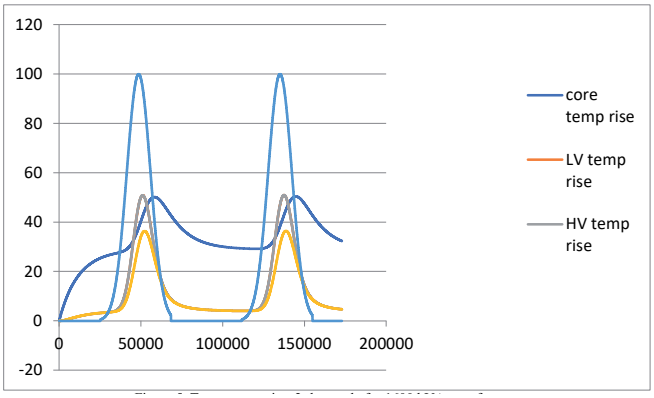

Fig. 5. Temperature rise, 2-day cycle for 1600 kVA transformer.

An overload factor is then applied. The goal is to see how much peak load we can apply and still be safe with regards to temperature. We are going to evaluate the existing design with two insulation systems: a mineral oil/cellulose system and aramid/synthetic ester system. This means in a first step, there is no evaluation of an optimized transformer with different insulation material. This will be done in a next stage.

Ramazan Altay, İrem Hazar, Mahmut Aksoy, Hakan Aktay, Jean-Claude Duart, Radoslaw Szewczyk, Development of transformers with natural ester and cellulose or aramid insulation, Journal of Energy, vol. 72 Number 3 (2023), 14–21
https://doi.org/10.37798/2023723506

TABLE VI

TEMPERTURE RISE FOR NO OVERLOAD AND SHORT TERM OVERLOAD CONDITIONS

	No overload				Short term overload		
	Winding rise	Top oil rise	Hotspot rise	Overload factor	Top oil rise	Hotspot rise	Overload factor
Mineral oil / cellulose	64	57	77	1.13	74	102	1.31
Synthetic ester / aramid	102	89	122	1.44	99	136	1.52

The Table VI shows the possible overload if we replace in the existing design the insulation and/or oil. The values in yellow are the limiting values. The existing design can have a peak load of 1.13 times 1600 kVA. With the existing load cycle, the temperatures would still be safe. If we would have filled the transformer with synthetic ester and insulated with aramid paper and board, we could load the transformer with a peak load of 1.44x1600. Similarly, we can apply the short- term overload criteria for evaluating the maximal peak load. It has to be stressed that just replacing the insulation structure and the oil is not really an optimal design. Basically, this means at this moment that the optimal 1600 kVA (mineral oil / cellulose) transformer can be overloaded with no ageing with a factor 1.13. The non-optimal synthetic ester / aramid can be overloaded with a factor 1.44. It also needs to be mentioned that the short-term overload situation results in considerable ageing in the case of mineral oil / cellulose, while in the ester / aramid combination there is still no aging. In a next step we need to evaluate optimal designs of every insulation combination.

6. *Comparison of optimal designs*

The 1600 kVA transformer with different insulation structures is then optimized and the possible overload factor for a derated transformer that would have the same losses and impedance as the 1600 kVA is used. The initial transformer mineral oil-cellulose is already designed. In the Table VI, we saw that this transformer could be overloaded by a factor 1.13 without ageing and with a factor 1.31 if we allow short term overload temperatures. The overload factor without aging leads to the following calculation deriving the optimized design of 1400 kVA.

1600 / 1.13 = 1416, we round to the nearest 50 kVA so we optimize the design to 1400 kVA. While an optimize design with allowed short term overload will lead to a different optimized design of 1200 kVA. Then, the maximum temperature rises are derived from the calculation tool once using the design data of the transformer with a peak load of 1600 kVA. In the Table VII, the two combinations considered and allowed temperature rises are shown (ambient is considered maximum 40°C).

TABLE VII

TEMPERATURE RISE LIMITS FOR NO OVERLOAD AND SHORT-TERM OVERLOAD CONDITIONS

Insulation structure	No overload			Short-time overload	
	top oil	winding	hotspot	top oil	hotspot
Mineral oil / cellulose	60	65	78	75	120
Synthetic ester / aramid	90	125	150	100	180

After optimizing the two combinations at 1600 kVA, the temperatures were derived, applying the design in the load cycle calculator. Then overload factors were found (one for no aging and one for short term overload.) The resulting transformer ratings and their temperatures are depicted below. The temperature results shown in Table VIII are all based on a load of 1600 KVA.

TABLE VIII

TEMPERATURE LIMITS FOR SIMULATED RATINGS TO 1600 KVA

	Top oil	Winding	Hotspot
1600 kVA-60-65-78	46	51	62
1400 kVA-60-65-78	55	62	75
1200 kVA-60-65-78	66		94
1600 kVA-90-125-150	62	95	111
1400 kVA-90-125-150	74	108	127
1250 kVA-90-125-150	85		139

For example, a 1250 kVA-90-125-150 is a synthetic ester / aramid design, if loaded with a peak load of 1600 kVA and with the assumed bell-curve load, top oil would rise 85°C and hotspot would have a rise of 139°C (well below allowed limits). The values shown in bold are the values higher than what would be allowed for continuous condition. A mineral oil / cellulose design transformer 1200 kVA loaded at 1600 kVA would be reaching temperatures that would degrade dramatically the insulation system.

B. Simulation study of 70 MVA power transformer

In this study, electric field intensity distribution of 70MVA, 36/12 kV power transformer with natural ester and cellulose was investigated in ANSYS Maxwell V2022 R2 and the thermal effect of natural ester oil on the windings was investigated in ANSYS FLUENT V2022 R2. The three main dielectrics used in transformer insulation are: transformer oil, paperboard barrier, oil-impregnated paper. The relative permittivity is shown in Table IX.

TABLE IX

DIELECTRIC PROPERTIES IN FUNCTION OF TEMPERATURE

	Relative permittivity		
Temperature	25°C	90°C	130°C
Natural ester	3,3	3,0	2,9
Low density pressboard	4,4	4,4	4,5
High density pressboard	4,6	4,8	5,2

The assumptions made during the analysis are that the LV, HV and TAP windings are considered as a single cylinder with axisymmetric uniform tension. Conductors are rounded to a radius of 0.5 mm by rounding from the corners and

0.5 mm paper coating is given. The boundary condition taken for this finite element problem is the Dirichlet boundary condition. The limb, yoke and core are considered as the boundary and grounded. The transformer is subject to three main high voltage tests:

1. lightning impulse test,
2. short duration power frequency test,
3. long duration power frequency test.

This equivalent voltage level is referred to as the design insulation level (DIL) expressed in kV_{rms}. Thus, there is only one DIL inside the transformer at any one time, with maximum equivalent one minute power frequency voltage levels for four different tests. It is important to convert all these values to one minute power frequency test. The highest of these values is used as excitation for the HV winding during simulation. As shown in Table X, design insulation factors are taken for historical conversion factors. [6] Tables X and XIII for medium voltage transformers below 75 kV indicate that it can be assumed that the DIL used for mineral oil can also be used for esters.

Ramazan Altay, İrem Hazar, Mahmut Aksoy, Hakan Aktay, Jean-Claude Duart, Radoslaw Szewczyk, Development of transformers with natural ester and cellulose or aramid insulation, Journal of Energy, vol. 72 Number 3 (2023), 14–21
https://doi.org/10.37798/2023723506

TABLE X

DESIGN INSULATION FACTORS

Condition	DIL Factor
Lightning impulse	2,3
AC one-minute test level	1,0
AC one-hour test	0,8

This section presents the description of the numerical model that allow us to study the thermal phenomena that occur in the analysis platform. This model has been carried out using the ANSYS FLUENT 2022 software. Thereby, the governing equations and the boundary conditions of the fluid study applied to 2D section of the winding are used. Also, computational domain, meshing and material properties are shown. Winding loss outputs are used as inputs for thermal analysis. While evaluating the losses, I2R+Eddy losses were evaluated homogeneously as total losses. The loss values used are as follows in Table XI.

TABLE XI

LOSS VALUES

75°C	I^2R (kW)	Eddy Loss (kW)
LV Winding	100	5,5
HV Winding	141	12,2

Many properties of ester oils, such as viscosity, conductivity, and thermal capacity, differ from mineral oils. Table XII details some of those properties.

TABLE XII

FLUID PROPERTIES

	Mineral Oil	Ester Fluid
Flash Point (°C)	110–175	250-310
Fire Point (°C)	110-185	300-322
Kinematic Viscosity (cSt) (90°C)	2,3	7-8
Density (kg/dm3) (20°C)	0,83-0,89	0,9-1,0

Due to installation of the transformers in southern region of Turkey, it was critical to consider impact of higher ambient temperatures. The annual temperature distribution of this region is examined, and thermal analyses are completed according to the climate conditions in that specific area of Turkey. The results of the simulation should present the changes with different ambient temperature considerations. The finite volume-based numerical method solves the Navier–Stokes equations, which state the conservation of mass, momentum and energy for a fluid flow. For an incompressible fluid (oils can be considered this way), the equations that state mass, momentum, and energy conservation are equations (2), (3) and

(4). On the other hand, for the solid domain, the equation that state energy conservation are:

$$\nabla\cdot(\rho u) = 0 \quad (2)$$

$$(u\cdot\nabla)\rho u = -\nabla p + \mu(\nabla\, 2\, u) + g\rho \quad (3)$$

$$\nabla\cdot(\rho C_p u T) = \nabla\cdot(k\nabla T) + q_s \quad (4)$$

$$0 = \nabla\cdot(k\cdot\nabla T) + q_s \quad (5)$$

Where ρ, ρ_{ref}, u, p, μ, g, C_p, T, k, and q_s of equations (2), (3), (4) and (5)) are density, density of reference, velocity vector, pressure, dynamic viscosity, gravity, specific heat capacity, temperature, thermal conductivity, and heat source, respectively. The right-hand terms of (3) are the pressure force, the viscous force, and the buoyancy force, respectively. The latter represents the force that drives the flow in natural convection regime, and it is related to density gradients in the fluid. This equation helps to represent the natural convection effect in computational fluid dynamics.

IV. DEVELOPMENT OF ADVANCED TRANSFORMERS

Integrating new materials in a design is always challenging as new applications require validation. The 70 MVA,

36/12 kV power transformer design is chosen for design optimization. The insulation structure in 70 MVA power transformer is showed in Fig.6.

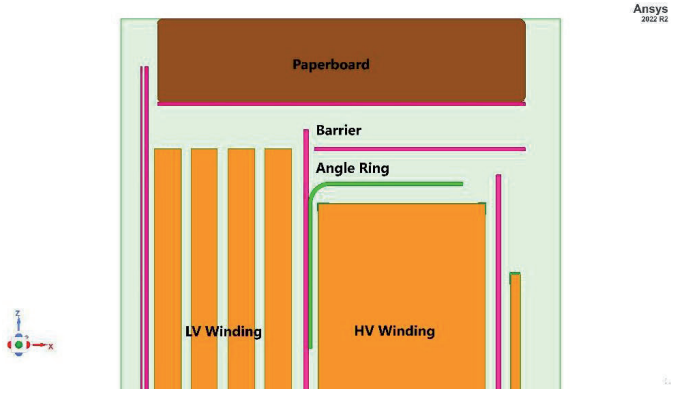

Fig. 6. Insulation structure of 70 MVA transformer.

The potentials of transformer core, tank and LV windings are defined as 0 kV, thereby regarded as grounded during the 1 min induced voltage test. Voltage is applied to the HV winding at the rate of the Design Insulation Level (DIL) coefficient. Safety factors are calculated by means of DIL factor for BIL. These are based on attached graph "DIL Factor" (from document "AC Insulation Design…" [7]) and can be derived by the equation (6):

$$\text{BIL Factor} = \text{BIL} / \text{AC} \Rightarrow 2.3 \quad (6)$$

TABLE XIII

FACTORS FOR CONVERSION TO ONE MINUTE (RMS) POWER FREQUENCY LEVEL

Test voltage	Multiplication factor
Lightning Impulse Level (BIL)	~ (1/2.30)=0.44
Switching Impulse Level (SIL)	~ (1/2.80)=0.55
Long Duration (one hour) Power Frequency Voltage	~ (1/0.80)=1.25

After calculation of DIL for 70 MVA, the transformer the one-minute power frequency voltage 73.913 kV is taken as excitation for calculating. Finite element electric field analysis is performed using the aforementioned boundary conditions at the main insulations for the design. Then, voltage and electric field distribution plots are shown in Fig. 7 and Fig. 8.

Historical limit curves shown in Fig. 9 are used for the AC analysis. When we inspect the reference table, A4I-5 limit curve is indicating the protection level due to isolation paper and A4I-6 limit curve is indicating the protection level due to barriers. We are using the A4I-6 limit curve as this is the safer protection level.

Safety margins in windings middle part (HV-LV) for 1 minute dielectric AC test are listed below. These margins are obtained by comparing calculated values by Finite Element analysis with the historical oil breakdown curve. These margins are obtained by comparing calculated values (red colored) of FEM analysis with the Weidmann oil breakdown curves (black colored). For oil duct numbering, please follow the direction on red colored streamlines. The main principle for oil duct numbering is that the direction of arrows is always from higher potential to lower potential. It means that direction is from right to left between HV/LV windings. Additionally, stress values on oil duct between HV and LV winding are obtained from Fig. 10 (red colored). The analysis results are below the current values and in the safe zone:

Ramazan Altay, İrem Hazar, Mahmut Aksoy, Hakan Aktay, Jean-Claude Duart, Radoslaw Szewczyk, Development of transformers with natural ester and cellulose or aramid insulation, Journal of Energy, vol. 72 Number 3 (2023), 14–21
https://doi.org/10.37798/2023723506

Oil Duct 1 - 65,25 % safety factor,

Oil Duct 2 - 61,14 % safety factor.

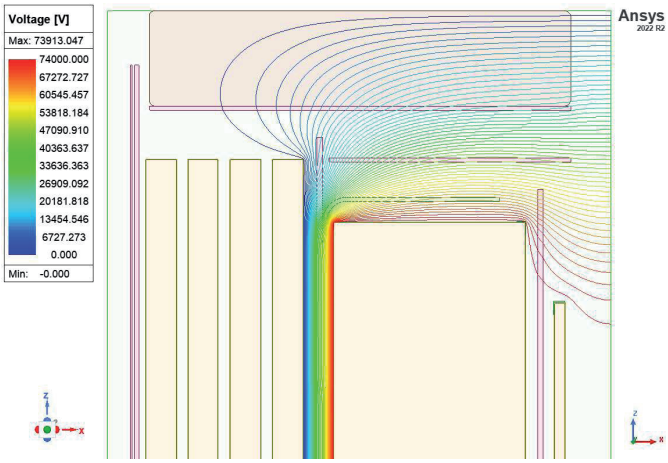

Fig. 7. Voltage distribution.

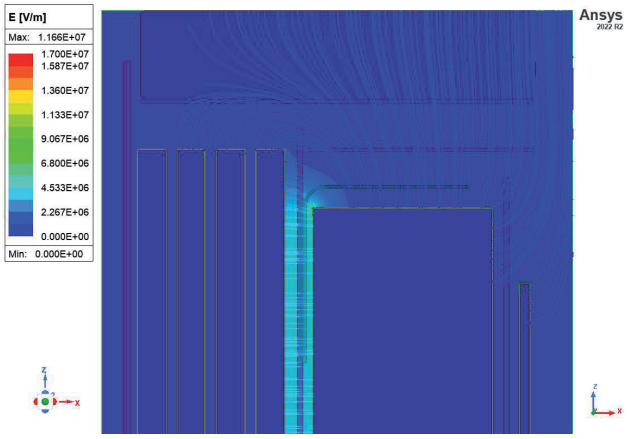

Fig. 8. Electrical field distribution.

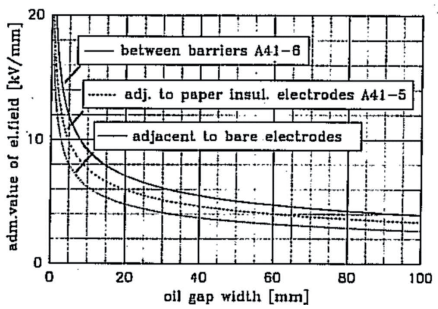

Fig. 9. Historical field distribution limits.

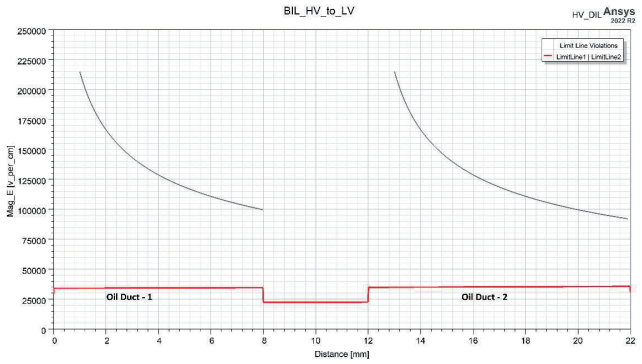

Fig. 10. Oil stress distribution and safety factors between HV winding and LV winding.

Thermal analysis was made separately according to mineral oil and ester liquid, the ambient temperature of 20°C and 40°C in order to see the effect of different ambient temperatures and different liquids. In each case, the maximum temperature is on the 1st layer of the LV winding. In the worst case of ester, the maximum gradient is 29 K for LV winding and 26 K for HV winding. Average gradients were obtained as 19 K for LV winding and 15 K for HV winding in the ester case. Within the scope of the project, the hot spot was also examined. For the 70 MVA LV winding, the hot spot was clearly visible on the first layer. The 70 MVA HV winding was also located on the first layer, but the 2nd, 3rd, 4th and 5th were also close to hot spot temperatures. The LV winding hot-spot value is about 8 K higher than the HV winding hot-spot value. The 70 MVA power transformer with ester CFD analysis results are shown in Table XIV. Table XV shows the mass flow distribution between the LV winding and HV winding.

TABLE XIV

CFD RESULTS FOR 70 MVA TRANSFORMER

		Average gradient (K)	
		LV	HV
Ambient Temp °C	20	19,25	15,25
	40	14,81	12,01

TABLE XV

MASS FLOW DISTRIBUTION RESULTS FOR 70 MVA TRANSFORMER

	LV	HV
Mass flow (% kg/s)	36	64

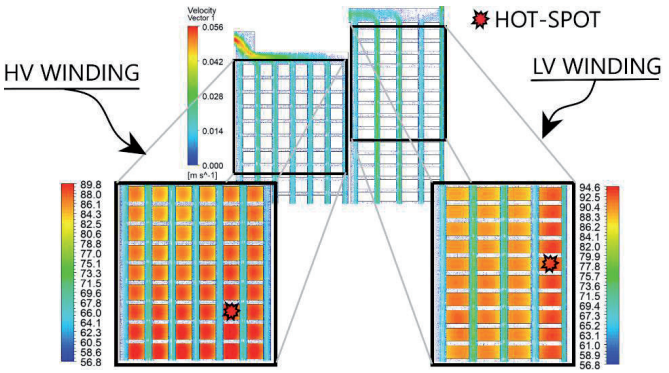

Fig. 11. Hot spot locations.

The comparison of different liquids has also been carried out in scope of this project. Due to lower viscosity advantages of mineral oils, the hot spot and average temperature results were better in mineral oil case. Average temperature rise and hot-spot were higher by 3 K and 6 K respectively, due to the use of the ester liquid instead of mineral oil in the LV winding CFD simulation model. The region with the maximum temperature increase (worst-case) is seen on the 1st layer of the LV winding. The hot spot location is expected in 75 mm below from 1st layer of the LV winding and 110 mm below from 2nd layer of the HV winding as shown in Fig. 11.

V. CONCLUSION

The work conducted on the development of advanced transformers with alternative insulation systems required a thorough analysis on how these materials can be integrated in the design. Whether we consider small distribution transformers (below 10

Ramazan Altay, İrem Hazar, Mahmut Aksoy, Hakan Aktay, Jean-Claude Duart, Radoslaw Szewczyk, Development of transformers with natural ester and cellulose or aramid insulation, Journal of Energy, vol. 72 Number 3 (2023), 14–21
https://doi.org/10.37798/2023723506

MVA, below 66 kV) or larger power transformers, studies are required to allow for an optimized use of such materials. Studies show that integrating such material can provide significant benefits in terms high loading capabilities without loss of life for transformers in PV solar installations or improve environmentally the large power transformers.

References

[1] R. Szewczyk et al., "Design of innovative resilient transformers for maximum operating flexibility", *CIGRE Session 2022*, Paper A2-11022

[2] R. Szewczyk et al., "Thermal faults simulation for aramid insulation in liquid immersed power transformers", *CIGRE Session 2022*, Paper D1- 11027

[3] J. Leung et al., "Solar power plant harmonic emission – design and commissioning case study", *Solar Integration Workshop,* Dublin, Ireland, 2019

[4] "Loading transformers with non-sinusoidal currents, ABB, Doc. 1LES100070-ZB, rev. 1, 2007

[5] K. Karsai et al., "Large power Transformers", Elsevier, 1987

[6] S. V. Kulkarni, S. A. Khaparde, "Transformer engineering: design, technology and diagnostics", CRC press, 2017

[7] D. J. Tschudi, "AC insulation design: paper-oil insulation systems", WICOR Insulation Conference, Rapperswil, Switzerland, 1996

Journal of Energy

VOLUME 72 Number 3 | 2023

journal homepage: http://journalofenergy.com/

Development of Fiber Reinforced Compound Bipolar Foils for Fuel Cells

Ali Osman Erdem, Paul Stannek, Marco Grundler, Alexander Nuhn, Stefan Schmidt, Sebastian Schmeer

***Summary* — In the research project »InduRex«, the challenge was to produce graphite polymer bipolar plates with the thinnest possible thickness. The physical and chemical requirements were defined according to the values set by the »Department of Energy«. Within the scope of the project, the continuous production of highly filled foils, which were then successfully structured as bipolar foils and operated in a fuel cell, was successfully implemented. Initial cell tests demonstrated a good cell efficiency at low and medium current densities. For this reason, the approach of creating bipolar plates from compound foils is still being pursued. Now the challenge is to produce bipolar films with a larger active area and to increase the mechanical stability to such an extent that the construction of a multicell stack can be realized. As a result, a metallic bipolar plate design was successfully transferred to a compound foil as part of the »InduRex« project. The problem is that with a larger bipolar foil there is a risk of obtaining low mechanical stability. Therefore, carbon fibers are introduced into the films as part of the research project »Faserverstaerkte Folien« in order to improve the mechanical properties. In addition to continuous production, the thin-walled foils are reinforced with carbon fibers using a hot press. The fiber-reinforced foils will be characterized in the next steps to investigate the influence of the carbon fibers. The aim is to obtain even thinner bipolar plates with consistent properties from the extruded foils in order to reduce the overall weight and volume of the fuel cell.**

***Keywords* — bipolar foils, fuel cell, compound, electrically conductive, highly filled, extrusion**

I. Introduction

Within a fuel cell (FC) stack, bipolar plates (BPP) are the largest volume unit and thus decisively define the resulting size of the stack, the weight and at least 30% of the cost. [1,2]. A low wall thickness of the BPP is therefore desirable, especially for mobile applications, so that metallic BPP are used almost exclusively for automotive FCs. However, metallic BPPs have the disadvantage that their service life is shorter due to corrosion and they have to be coated in advance at high cost. Graphitic or compound-based BPPs, on the other hand, do not need to be coated and currently achieve a longer service life than metallic BPPs [3]. Strategic Analysis Inc. has done a costing exercise for fuel cell systems using metallic and graphitic BPP in [4]. This shows, among other things, that the costs with graphitic BPP result at ~ $3/kW and metallic BPP at ~ $6/kW for light duty vehicles at a produced unit rate of 500,000 systems/year. Thus, FC systems with graphitic BPP meet the Department of Energy (DoE) target for specific cost [5]. However, graphitic BPP are usually significantly thicker (~ 2.3 mm) than metallic BPP (~ 0.1 mm or ~ 0.4 mm formed) due to the „classic“ manufacturing processes such as hot pressing or injection molding. Using the production process of foil extrusion presented here, highly filled compound-based unstructured bipolar half-panels (BPHP) can be produced continuously in thicknesses as thin as 0.37 mm. The reduction of the thickness compared to injection or compression molded BPP leads to a significant reduction of the weight and volume of the final FC stack. Also, the reduction of the raw materials needed to produce a BPP saves costs and reduces the carbon footprint. With the addition of carbon fibers, even very thin foils can obtain the required mechanical stiffness.

(Corresponding author: Ali Osman Erdem)

Ali Osman Erdem, Paul Stannek, and Marco Grundler are with the Compound Technology – Fuel Cell & Stacks, The Hydrogen and Fuel Cell Center, Duisburg, Germany (e-mails: a.erdem@zbt.de, p.stannek@zbt.de, m.grundler@zbt.de)

Alexander Nuhn, Stefan Schmidt, and Sebastian Schmeer are with the Component Development – Mechanical Characterization & Modeling Leibniz-Institut für Verbundwerkstoffe GmbH, Kaiserslautern, Germany

(e-mails: alexander.nuhn@ivw.uni-kl.de , stefan.schmidt@ivw.uni-kl.de, sebastian.schmeer@ivw.uni-kl.de)

II. Methodology

Thin-walled bipolar foils are produced at ZBT on a Brabender KE 30 single-screw extruder with a coupled sheet die and downstream calendaring unit from Saueressig (Fig. 1).

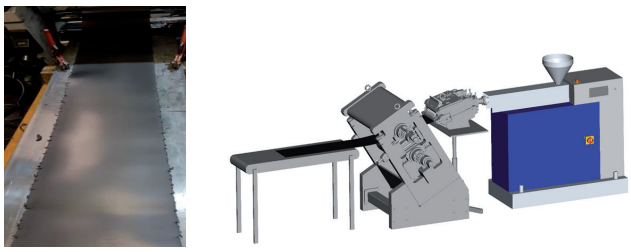

Fig. 1. Calendered bipolar foil and production line

For foil production with the production line shown in Fig. 1, compound material is first produced on a ring extruder (Extricom RE3). In this process, the matrix polymer (polypropylene) is fed into the extruder upstream via a dosing differential scale, melted and loaded downstream with various fillers, mainly graphite and conductive carbon black. The choice of fillers and the ratio of matrix polymer to fillers is decisive for the physical properties of the compound materials and the subsequent bipolar foil. Due to the

Ali Osman Erdem, Paul Stannek, Marco Grundler, Alexander Nuhn, Stefan Schmidt, Sebastian Schmeer, Development of Fiber Reinforced Compound Bipolar Foils for Fuel Cells, Journal of Energy, vol. 72 Number 3 (2023), 22–28
https://doi.org/10.37798/2023723498

increase in viscosity and the change in mechanical properties with an increase in filler content, the compound formulation has to be adapted to the foil production process.

The previously produced compound is transferred to the feed hopper of the single-screw extruder, melted and conveyed to the sheet die. There, the melt emerges with a width of 250 mm and, due to the variable cleft lip of the die, the thickness can be adjusted between 0.4 mm and 1.5 mm. The downstream calender specifies the final thickness of the bipolar foils via a variable roll gap. The unstructured bipolar foils produced in this way are subjected to numerous characterizations ex-situ (electrical resistance, hydrogen permeation and mechanical parameters). For mechanical characterization tensile tests were performed. Dogbone specimens of 0.4mm thickness were laser cut (speciment type 1B of DIN EN ISO 527-2) and tested in a Zwick 1485 testing machine. Strain measurement was done optically via digital image correlation using the Software GomCorrelate.

Some foils are reinforced with carbon fibers by hot pressing in previous steps to increase mechanical stiffness. These are also characterized ex-situ and compared with the foils without fiber reinforcement to determine any influence of the carbon fibers. The following results relate to two different carbon fiber-reinforced semi-finished products used to reinforce foils:

- 15K carbon fiber roving TR 50S from Mitsubishi, with binder resin (EPIKOTE Resin TRAC 06720) with 8 w% spread to 20 mm width.
- CFR-UD tape Tafnex CF-PP 66 w%, thickness: 0.16 mm

The mold used is a polished 50 mm sample mold consisting of a stamp and guide sleeve, see Fig. 2. The system technology for temperature control and pressure application is a variothermal laboratory press, see Fig. 3. The release agent Frekote 55-NC from Loctite and an additional fabric-reinforced PTFE release foil are used to separate the tools.

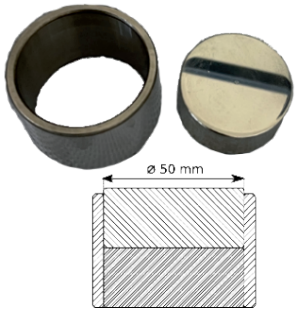

Fig. 2. Polished press body for 50 mm samples

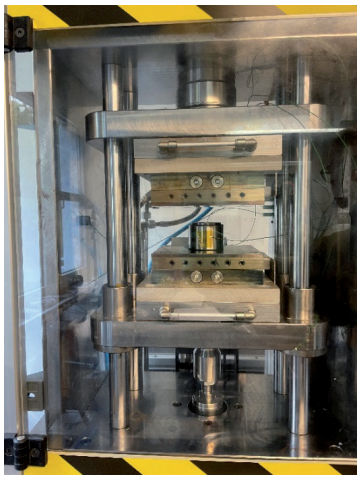

Fig. 3. Laboratory press with pressing tool

The pressing process is divided into three phases: firstly the heating phase (Time: 0 to 5 minutes), secondly the pressing phase with constant temperature and constant pressure (Time: 5 to 15 minutes) and thirdly the cooling phase (Time: 15 to 25 minutes), see Fig. 4.

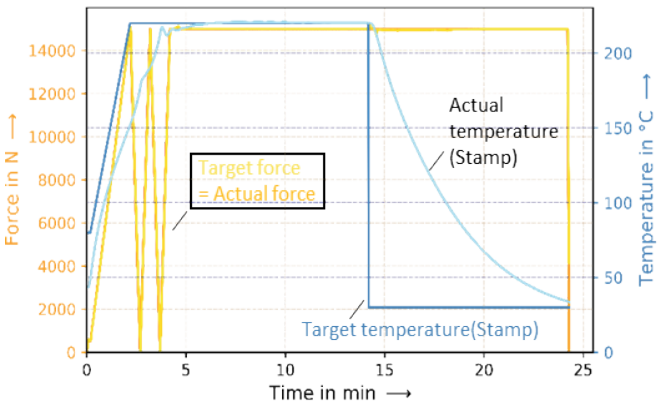

Fig. 4. Variothermal process control

During the first phase, the mold is heated via the heated pressing plates and the pressing force is applied. The mold cavity reacts to the temperature change with a time delay due to its own thermal resistance and adapts to the controlled temperature of the press plates. The tool starts at 40 °C and is heated to 220 °C within 5 minutes. The pressing force is relieved twice during heating to prevent the press plunger from jamming in the tool.

The closed cavity creates a pressure build-up of around 7.6 N/mm² with a pressing force of 15 kN on the samples. This pressure is maintained in the second phase at a constant 220 °C for about 10 minutes.

In the cooling phase, the sample is cooled to 40 °C under constant working pressure, then relieved and demolded. It should be noted that due to the precise control of the press, the measured pressing force overlaps with the specified target force, so that only one line (yellow/orange) is visible in the diagram.

Micrographs:

The molded specimens for the micrographs are embedded in EpoFix Resin plus EpoFix Hardener from Struers. They are then ground on an ATM Saphir 360 grinding disc with water cooling and grit sizes from 180 to 4000. This is followed by polishing stages with 3 and 1 ym on an ATM Saphir 320. The micrographs are taken with a Leica DM6000M reflected light microscope.

In order to also characterize the bipolar foils in-situ in a Baltic Fuel Cell test hardware, flow fields were transferred into the bipolar foils using the embossing die shown in Fig. 5 and a laboratory press from Höfer. For this purpose, the bipolar foil is heated to the melt temperature of the polymer used and then an embossing force of 50 kN is applied to the flow field area of 25 cm².

After the cell made of compound bipolar foils had run successfully, developments for a cell with a larger active area followed. Within the "InduRex" project, it was possible to transfer the design of a metallic bipolar plate to a compound bipolar foil. The decisive factor was to adapt the design in such a way that the cell could be sealed. During the hot press process, it was first necessary to adjust the parameters so that no cracks occurred and the structures were mapped evenly. Analogous to the 25cm² single cell design, the structures were incorporated into the compound foil by means of the hot press process. The following Fig. 5 shows the compound bipolar foil with an active area of 100 cm².

Ali Osman Erdem, Paul Stannek, Marco Grundler, Alexander Nuhn, Stefan Schmidt, Sebastian Schmeer, Development of Fiber Reinforced Compound Bipolar Foils for Fuel Cells, Journal of Energy, vol. 72 Number 3 (2023), 22–28
https://doi.org/10.37798/2023723498

Fig. 5. Compound foil BPP with an active area of 100 cm²

Initially, the construction and operation of a single cell is planned. With conventional metallic bipolar plates, cooling takes place between the bipolar half-plates. The cooling concept of metallic bipolar plates is not directly transferable to the compound bipolar foils. The compound bipolar foils are structured on one side and embossed flat on the other. This eliminates the cooling function between the bipolar plates. For the single-cell design, cooling was therefore planned through the insulation plate. The cell is sealed with the help of gaskets that are inserted into the grooves in the insulation plate and the dispenser gaskets applied to the bipolar foils. The final assembly is done by threaded rods, which are fastened with nuts. The following Fig. 6 shows the individual components for the assembly of the cell.

Fig. 6. Components for the assembly of the single-cell unit with an active area of 100 cm²

There are also challenges with the single-cell compound bipolar foils. An alternative solution for cooling will have to be found for a multi-cell setup. The presented setup only works as a single cell. It would be conceivable to weld or glue the bipolar foils together. Another alternative would be to emboss the compound foil on both sides to distribute the media on one side and to enable cooling on the other. In the following sections, the embossing of compound foils on both sides will be discussed again.

Another problem is the mechanical stability of the compound bipolar foils. The bipolar foils must be tensioned with a defined contact pressure to enable the best possible contact with the GDL. The mechanical strength of the bipolar foils should be sufficient to prevent them from breaking or cracking. This problem increases in the case of an assembly with several cells, because there is a potential risk of misalignment and homogeneous compression of the fuel cell stack is made more difficult. As already mentioned, the „Faserverstarrkte-Folien“ project is attempting to strengthen the mechanical strength of compound films with the help of carbon fibers. Therefore, a 25cm² single cell testwith fiber-reinforced foils is being carried out as part of the „Faserverstaerkte Folien“ project to test the effect of the fibers.

III. Results

Since the beginning of the research project, numerous bipolar foils have been produced from various material formulations and characterized with regard to their physical and chemical properties. Excerpts of the measurement results are presented below.

A. Electrical Resistance of unreinforced foils

The bipolar foils were measured with regard to the area-specific contact resistance relevant for FC applications. A specially constructed test stand was used to measure the resistances. As shown in Fig. 7 the sample is clamped between two gold-plated copper poles (A = 4 cm²) whose contact pressure can be controlled linearly by compressed air. A gas diffusion layer (GDL), whose contact force or pressure-dependent resistance curve is known, is previously applied to each of the measurement poles, whereby the measurement section is oriented very closely to the real resistance chain in a fuel cell [6].

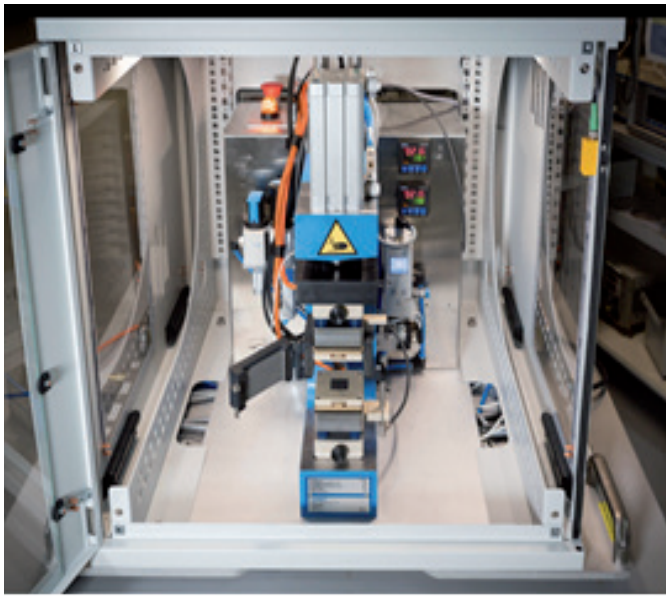

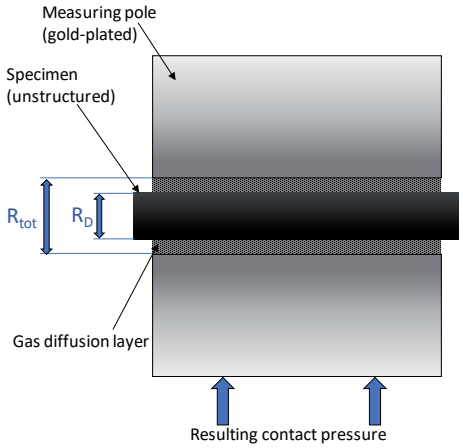

Fig. 7. BePPel resistance test rig (top) and measuring principle (bottom)

For the project “Faserverstaerkte Folien”, in order to reinforce compound foils with fibers, four different compound foils were produced as matrix material with different filler contents. Foils with 23% polymer content, 28% polymer content, 27% polymer content and 30% polymer content were produced. The selected raw materials of Mat.1 and Mat.2 differ from the rest of the foils, whereas Mat.3 and Mat.4 were produced from the same raw materials. These were first measured for area resistivity to determine their suitability as bipolar plate material, as shown in Fig. 8 below. The compound foils were measured in the untreated, ground and then annealed state. It can be clearly seen that by optimizing the material composition and filler content, the area-specific forward resistivity was reduced from, for example, 45 mΩcm² with a polymer content of 23% down to 12 mΩcm². However, the aspect of further

Ali Osman Erdem, Paul Stannek, Marco Grundler, Alexander Nuhn, Stefan Schmidt, Sebastian Schmeer, Development of Fiber Reinforced Compound Bipolar Foils for Fuel Cells, Journal of Energy, vol. 72 Number 3 (2023), 22–28
https://doi.org/10.37798/2023723498

post-processing or fiber incorporation has to be considered. Therefore, the experiments of fiber insertion are tested with foils of Mat.4. The reason for this is that due to the lower filler content or higher polymer content, the flowability is higher and therefore the fiber incorporation is facilitated.

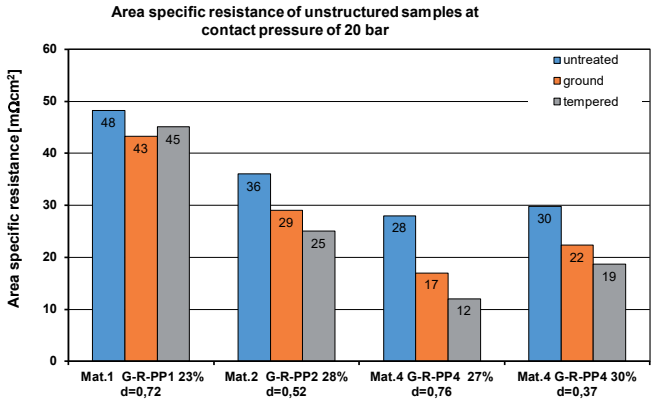

Fig. 8. Area-specific contact resistances of unstructured bipolar foils

B. Mechanical characterization

Stress strain curves of the unreinforced compound foils (Fig. 9) show the strong embrittlement of the polypropylene by incorporation of graphite and carbon black. The values for fracture strain, tensile strength and elastic modulus (measured between 0 and 0.1% strain due to strong non-linearity after 0.1% strain) are 0.48 ± 0.05%, 38.6 ± 1.7 MPa and 11.1 ± 0.4 GPa respectively. Therefore, the fillers reduce the polypropylen's fractures strain drastically from about 700% to about 0.5%. Conversely, the elastic modulus is increased roughly tenfold. Ultimate tensile strength is increased by about 14%.

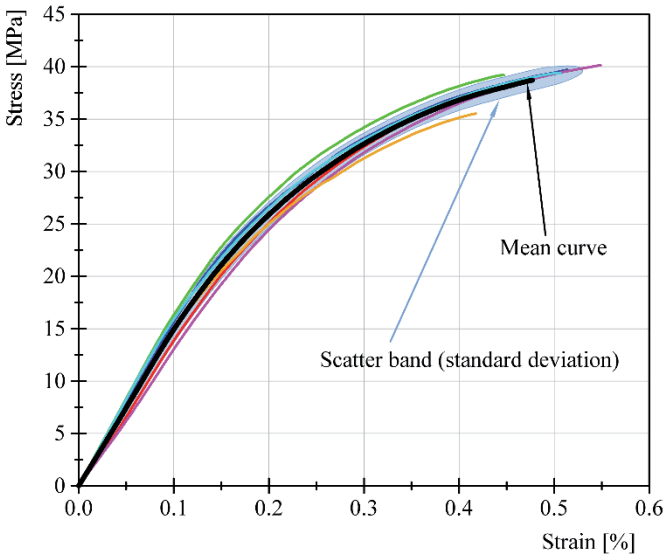

Fig. 9. Stress strain curves of unreinforced compound foils + mean curve and scatter band (standard deviation).

C. Fiber application in the pressing process and micrograph analysis

As part of the project, C-fibers were incorporated in various orientations on and in the compound foils to improve mechanical stability. These samples can be taken from the two following figures.

Fig. 10 shows samples 7 and 13 before impregnation. The UD tapes on the bipolar foil (left) and the spread C-fibers with impregnating powder between the fibers are clearly visible. The powder is milled compound from G-R-PP75%

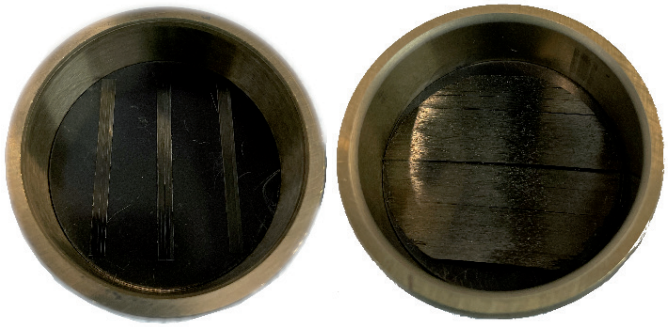

Fig. 10. Sample 7 and 13 before pressing

The compressed and demolded specimens are shown in Fig. 11

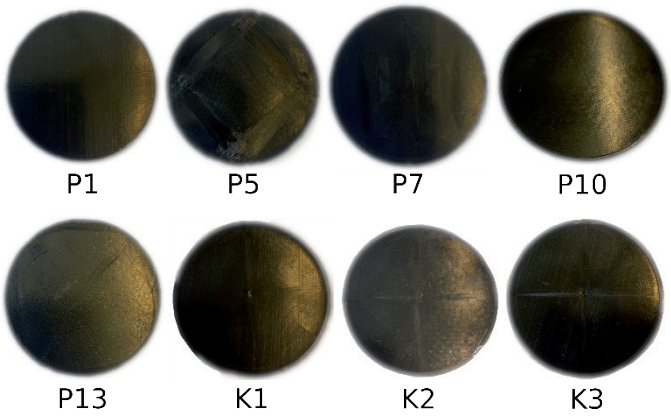

Fig. 11. Fiber-reinforced samples P1, P5, P7, P10, P13 and K1, K2, K3. Diameter of the samples: 50 mm

The following table 1 contains a detailed description of the various samples and their configuration.

Table 1

Produced Fiber Reinforced Compound Foils

Sample	Layer	Fiber type	Fiber size	Press parameters
1	foil + foil	none	none	220°C & 15 kN
5	foil + foil + foil	CF-PP strip	2.5 mm wide	220°C & 15 kN
7	foil + line + foil + line	CF-PP strip	2.5 mm wide	220°C & 15 kN
10	foil + splayed + foil	splayed C-fibers	whole area	220°C & 15 kN
13	milled + splayed + foil + milled	splayed C-fibers	whole area	220°C & 15 kN
K1	foil + hashtag + foil	CF-PP strip	1.1 – 1.2 mm	220°C & 15 kN
K2	foil + hashtag + foil	CF-PP strip	1.5 – 1.6 mm	220°C & 15 kN
K3	foil + hashtag + foil	CF-PP strip	2.1 – 2.3 mm	220°C & 15 kN

foil | hashtag fiber pattern | line fiber pattern | splayed fiber | milled compound

It can be noted that only the conventional CF-PP tapes achieve good adhesion to the bipolar plate due to their surplus matrix. At the same time, an electrically insulating separating layer is formed, see Fig. 12.

Ali Osman Erdem, Paul Stannek, Marco Grundler, Alexander Nuhn, Stefan Schmidt, Sebastian Schmeer, Development of Fiber Reinforced Compound Bipolar Foils for Fuel Cells, Journal of Energy, vol. 72 Number 3 (2023), 22–28
https://doi.org/10.37798/2023723498

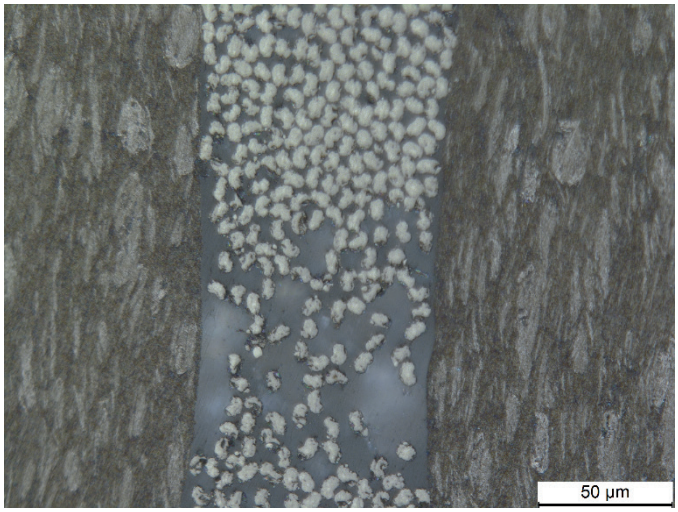

Fig. 12. Micrograph of sample 7 showing the bipolar film at the edges and the interface of the CF-PP tape in the center.

The reduction of this separating layer through the use of spread fiber layers plus milled compound, as in sample 13, shows the lowest fiber-reinforced layer thickness of all samples. Minimum layer thicknesses in the order of up to 2-3 carbon fiber diameters were achieved here, see Fig. 13. Due to the lower proportion of binder resin compared to the conventional UD tape, the C-fibers are much closer together. This leads to poor strength between the fibers.

It can also be seen that the PP matrix flows out of the bipolar plate and partially fills the free spaces between the fibers. However, this effect is not sufficient to achieve a good bond to the bipolar film and between the fibers. However, a relatively high electrical conductivity is achieved, taking into account 100% or full-surface fiber coverage.

Fig. 13. Micrograph of sample 13. The separating layer is approx. 2-3 carbon fiber diameters thick. The bipolar film is located on the sides.

D. Electrical Resistance reinforced foils

In order to investigate the influence of the fibers on the electrical conductivities, the area specific volume resistances of the samples from Fig. 11 were first measured.

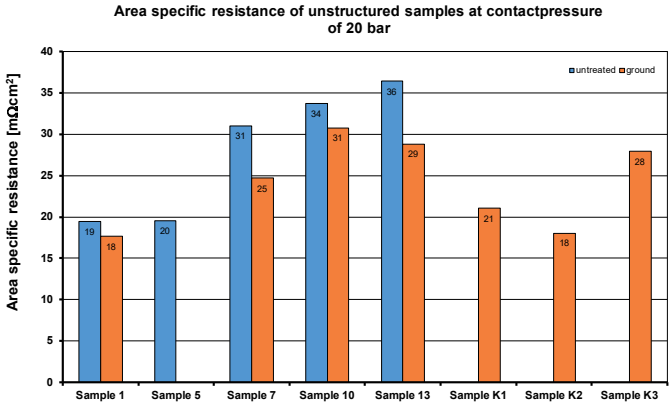

Fig. 14. Area-specific contact resistances of unstructured fiber reinforced foils

In the measurement shown in Fig. 14, two foils were pressed into one sample as the reference sample or Sample 1. The remaining samples are also two foils, but with fibers inserted between the foils.

Analogous to the foils without fiber reinforcement, the samples were each measured untreated and in the ground condition. Due to an uneven surface, the last three specimens could only be measured in the ground condition. Sample 5 could only be measured in the untreated state because fibers detached from the surface after grinding.

It can be seen in the Fig. 14 that the orientation and quantity of fibers significantly affects the area-specific forward resistivity. With the correct arrangement of the fibers and the optimal fiber size, it is possible to keep the resistances very low and in the same range as the reference sample, see sample K2 compared to the sample 1 in Fig. 14.

E. Hydrogen Permeation

The permeation measurements at ZBT are carried out in a cell-realistic manner by applying 100 % hydrogen to one side of a sample material. On the opposite side, the hydrogen concentration increase is measured after a defined time. The bipolar foil is positioned as shown in Fig. 15 and flooded with a hydrogen pre-pressure of 1 bar.

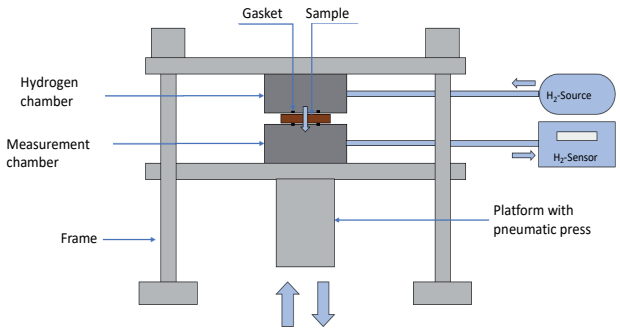

Fig. 15. H2 permeation test rig

To determine the suitability of the compound foils as bipolar plate material, a certain hydrogen impermeability must be achieved. Analogous to the DoE specifications, ZBT determines limit

Ali Osman Erdem, Paul Stannek, Marco Grundler, Alexander Nuhn, Stefan Schmidt, Sebastian Schmeer, Development of Fiber Reinforced Compound Bipolar Foils for Fuel Cells, Journal of Energy, vol. 72 Number 3 (2023), 22–28
https://doi.org/10.37798/2023723498

values for permeation coefficients in order to evaluate the impermeability. These limit values can be taken from the following table 2. Therefore, the target is to obtain a permeation coefficient less than 10 E-8 cm²/s.

TABLE II

LIMITING VALUES OF PERMEATION COEFFICIENTS FOR SUITABILITY AS BIPOLAR PLATE MATERIAL

Rating	excellent	very good	good	partially acceptable	only sealing material
Perm. coeff. [10E-8 cm²/s]	<0,1	<1	<10	<100	< 1000

The compound foils, which were manufactured for the fiber reinforcement, were tested for hydrogen tightness using the test rig shown in Fig. 15 and the results can be seen in Fig. 16.

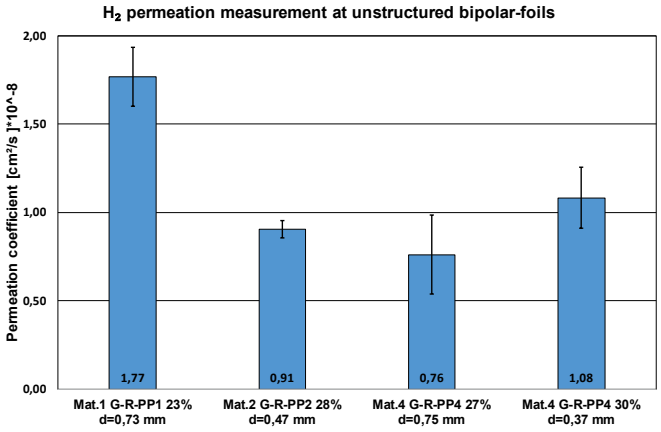

Fig. 16. Permeation coefficients of unstructured bipolar foils

As shown in the figure, all material compositions have a permeation coefficient lower than 10 E-8 cm²/s and even less than or equal to 1 E-8 cm²/s. Therefore, all compound foils are suitable as bipolar plate material in terms of hydrogen impermeability.

First fiber-reinforced samples were also tested for hydrogen tightness and are shown in the following Fig. 17.

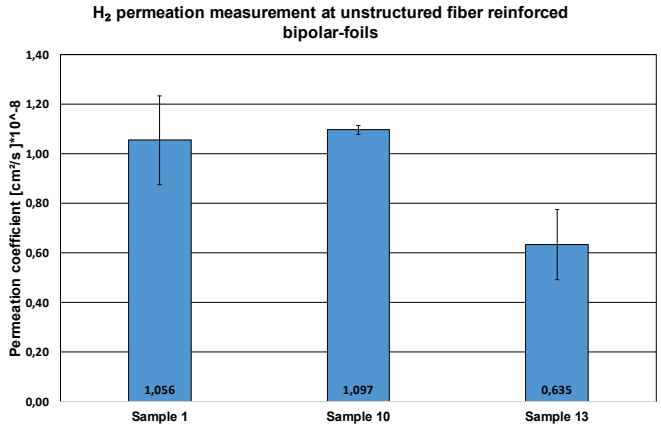

Fig. 17. Permeation coefficients of unstructured fiber reinforced bipolar foils

Analogous to the previous measurement, all samples are in the limit ranges less than or equal to 1 E-8 cm²/s and therefore suitable as fuel cell material.

F. EMBOSSING AND FIBER REINFORCEMEND

Within the project "Faserverstaerkte-Folien", the double-sided embossing of compound foils was first investigated. The foils were inserted between two structured stamps, each consisting of a positive and negative half, and hot pressed with suitable parameters. This made it possible to obtain a structured film with a homogeneous residual wall thickness. Within the project „Faserverstaerkte-Folien", the Leibniz Institute for Composite Materials GmbH was able to demonstrate that it is possible to emboss compound films on both sides and this is shown in the following Fig. 18.

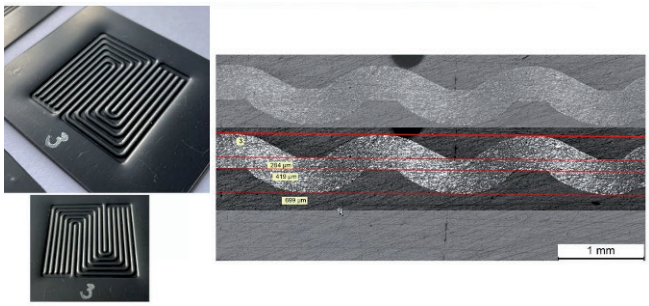

Fig. 18. Both side structured compound foil

To increase the mechanical strength of the compound foil, carbon fibers will be added to the structured foil due the hot press process. In the first steps the challenge is to obtain the right parameters to add the carbon fibers in the compound material without damaging the foil. Afterwards the challenge is to choose the right fibers with the optimal distribution without the deterioration of the function as a bipolar plate. In the following Fig. 19 a structured compound bipolar foil with added carbon fibers is shown.

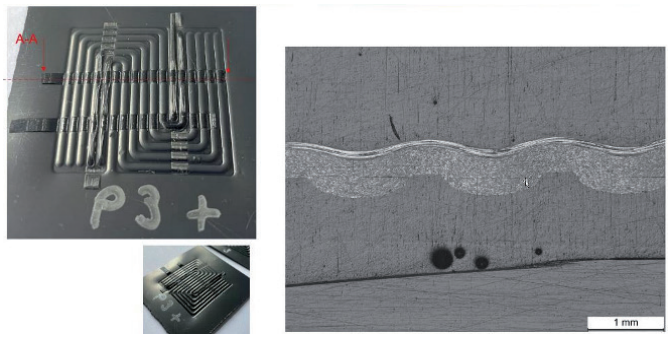

Fig. 19. Both side structured compound foil with carbon fibers

Using carbon fiber reinforcement, it is possible to assemble a fuel cell stack with several cells. However, the main aspect of fiber reinforcement is that it allows thinner foils to be used to reduce the overall weight and volume of the fuel cell stack.

IV. DISCUSSION

With the production process developed at ZBT, it is possible to continuously produce highly filled compound foils with thicknesses between 0.4 mm and 1.5 mm that are suitable for FC applications. The measurement methods and test rigs used had to be adapted to the significantly thinner bipolar foils. The test procedures were successfully modified so that the bipolar foils can be reproducibly characterized both ex-situ and in-situ. The investigations carried out show that the area-specific forward resistances of the most electrically conductive bipolar foils to date are lower than 20 mΩ in the unstructured state. The H2 permeation coefficients are higher compared to metallic and the much thicker injection-molded or hot-pressed compound-based BPHP, but can be evaluated as

Ali Osman Erdem, Paul Stannek, Marco Grundler, Alexander Nuhn, Stefan Schmidt, Sebastian Schmeer, Development of Fiber Reinforced Compound Bipolar Foils for Fuel Cells, Journal of Energy, vol. 72 Number 3 (2023), 22–28
https://doi.org/10.37798/2023723498

very gas-tight to hydrogen after adjusting the embossing parameters. The drastically low fracture strain of <0.5% demonstrates the need for fiber reinforcement to enable mechanical stability. However, for a comprehensive characterization mechanical tests also need to be performed at the operating temperature of a fuel cell of 80 °C. Strain is expected to increase for higher temperatures but strength and stiffness will drop significantly. Furthermore, the mechanical influence of the fiber reinforcement needs to be appropriately evaluated. Both evaluations will be performed in the course of this project. The fiber reinforcement applied by the IVW appears to implement the desired properties such as electrical resistance or hydrogen permeability and high strength in a favorable trade-off. In addition, locally applied conventional CF-PP tape was shown to be a good way of increasing strength with moderately increasing electrical resistances.

Acknowledgment

Funded by the Federal Ministry of Economic Affairs and Climate Action on the basis of a decision by the German Bundestag within the project 22342 N and 03ETB017B.

References

[1] Sharma, P.; Pandey, O. P. Proton exchange membrane fuel cells: fundamentals, advanced technologies, and practical applications. In *PEM Fuel Cells*:*Fundamentals, Advanced Technologies, and Practical Application*; Elsevier, 2022; pp 1–24. DOI: 10.1016/B978-0-12-823708-3.00006-7.

[2] Porstmann, S.; Wannemacher, T.; Drossel, W.-G. A comprehensive comparison of state-of-the-art manufacturing methods for fuel cell bipolar plates including anticipated future industry trends. *Journal of Manufacturing Processes* 2020, *60*, 366–383. DOI: 10.1016/j.jmapro.2020.10.041.

[3] Peter Bach. *Bipolar Plates: Carbon or Metal for PEM Fuel Cells?* https:// blog.ballard.com/bipolar-plates (accessed 2022-07-27).

[4] James, B. (2019). DOE Hydrogen and Fuel Cells Program Review Presentation: Fuell Cell Systems

[5] Department of Energy. *DOE Technical Targets for Polymer Electrolyte Membrane Fuel Cell Components*. https:// www.energy.gov/eere/fuelcells/doe-technical-targets-polymer-electrolyte-membrane-fuel-cell-components (accessed 2022-07-26).

[6] Verbundvorhaben NIP II - BePPel - Bipolarplatten für Brennstoffzellen und Elektrolyseure

Ali Osman Erdem, Paul Stannek, Marco Grundler, Alexander Nuhn, Stefan Schmidt, Sebastian Schmeer, Development of Fiber Reinforced Compound Bipolar Foils for Fuel Cells, Journal of Energy, vol. 72 Number 3 (2023), 22–28
https://doi.org/10.37798/2023723498

Journal of Energy

VOLUME 72 Number 3 | 2023

journal homepage: http://journalofenergy.com/

Simulated Thermal Fault: Assessing Dissolved Gas Analysis through Tube Heating Method on Mineral Oils and Natural Ester

Pär Wedin, Elena Minchak, Carl Wolmarans, Robert Fairholm, Jessica Singh, Kaveh Feyzabi, Thomas Norrby

***Summary* — Dissolved gas analysis (DGA) is the most widely used technique for monitoring transformer condition and detecting faults at an early stage. The quantity and type of gases that are produced by transformer faults and dissolved in the insulating liquid can reveal a lot about the nature and severity of the fault. To explore the variations in the dissolved gases based on the severity of the fault and the type of insulating liquid, we employed the Tube Heating Technique to simulate thermal faults at regulated temperatures up to 800 °C. To illustrate these differences, DGA data from commercially used insulating fluids such as inhibited and uninhibited mineral oils and a natural ester, will be presented.**

***Keywords* — transformer, dissolved gas analysis, DGA, thermal fault, mineral oil, natural ester**

I. Introduction

The universally accepted technique for monitoring the condition of transformers to detect faults at an early stage is dissolved gas analysis (DGA) [1]. Faults in the transformer often generate gases that are dissolved in the insulating liquid. The quantity and type of gases provide significant information about the nature and severity of the fault.

Analysis of the gases in insulating oils using the gas chromatography method offers the highest accuracy and repeatability compared to hydrogen online monitoring and photoacoustic spectroscopy [2]. Oil samples need to be collected from operational transformers, and after undergoing several procedures, the extracted gases are analysed in the laboratory through gas chromatography. Compared to laboratory analysis, online DGA in power transformers is an even greater tool for predictive maintenance and ensuring the reliable operation of these critical assets [3]. By regularly analysing the dissolved gases in real-time or near real-time, abnormalities can be detected early, allowing for proactive maintenance and preventing potential catastrophic failures [4]. This technology enables timely intervention, helps in planning maintenance schedules, minimizes downtime, and ultimately extends the operational life of the transformer. Moreover, it assists in making informed decisions about whether specific transformers need immediate attention or can continue in operation, optimizing resource allocation and enhancing overall grid reliability.

To enhance research on interpreting dissolved gases, particularly for testing the next generation of insulating fluids, the establishment of a small-scale laboratory setup to replicate thermal faults (hotspots) is desirable. One such setup involving a heating wire has been proposed to emulate thermal faults under small-scale laboratory conditions, within a temperature range of up to 550°C [5]. Another publication suggested utilising resistance heating as the heat source; however, this method only reached temperatures of up to 320°C [6]. Notably, achieving a stable thermal fault simulation at temperatures exceeding 400°C on a small scale has proven to be challenging. Nevertheless, the tube heating method emerged as a promising alternative for replicating conditions resembling thermal faults at temperatures of up to 750°C [7, 8]. While this method appears to be reliable for simulating stable faults, it is imperative to verify the extent to which results obtained through this approach can accurately correlate with findings from operational transformers. This verification process is crucial for advancing diagnostic knowledge.

This study presents the development of a testing system designed to examine thermal faults using the tube heating method. An inhibited mineral oil, an uninhibited mineral oil, and a natural ester were exposed to thermal faults up to 800°C, and the resulting gases were analysed using dissolved gas analysis. The outcomes are subsequently presented and juxtaposed with the essential gas ratios employed in IEC 60599 [9] for forecasting fault types in transformers.

II. MATERIALS AND METHODS

A. Investigated liquids

Three different insulating liquids were subjected to testing using the experimental rig. These liquids include an inhibited mineral oil (inhibited MO, NYNAS NYTRO 10XN), an uninhibited mineral oil (uninhibited MO, NYNAS NYTRO Libra), and a natural ester (NYNAS NYTRO 100 NE). Table 1 provides an overview of the principal physical properties of the analysed insulating liquids. The boiling point distribution for the mineral oils is illustrated in Figure 1. Prior to testing, the insulating liquids were filtered and de-gassed using vacuum-filtration with 1.2 µm filters.

(Corresponding author: Pär Wedin)

Pär Wedin, Elena Minchak, Carl Wolmarans, Robert Fairholm, Jessica Singh, Kaveh Feyzabi and Thomas Norrby are with the NYNAS AB, Stockholm, Sweden (e-mails: par.wedin@nynas.com, elena.minchak@nynas.com, carl.wolmarans@nynas.com, robert.fairholm@nynas.com, jessica.singh@nynas.com, kaveh.feyzabi@nynas.com, thomas.norrby@nynas.com)

Pär Wedin, Elena Minchak, Carl Wolmarans, Robert Fairholm, Jessica Singh, Kaveh Feyzabi, Thomas Norrby, Simulated Thermal Fault: Assessing Dissolved Gas Analysis through Tube Heating Method on Mineral Oils and Natural Ester, Journal of Energy, vol. 72 Number 3 (2023), 29–33
https://doi.org/10.37798/2023723503

TABLE I

OVERVIEW OF THE PHYSICAL PROPERTIES OF THE EXAMINED INSULATING LIQUIDS.

	Method	Uninhibited MO	Inhibited MO	Natural ester
Density at 20°C (kg/m^3)	ASTM D4052	879.0	874.3	914.6
Viscosity at 40°C (mm^2/s)	ASTM D445	9.295	7.638	40.59
Flash point, PM (°C)	ASTM D93A	153	142	275
Water content (ppm)	IEC 60814	4.4	3.1	41
Acidity (mg KOH/g)	IEC 62021-3	0.007	0.006	0.089
DDF at 90°C	IEC 60247	0.0004	0.0001	0.0096
IFT (mN/m)	ASTM D971	45.1	49.2	27.2
Color	ASTM D1500	<0.5	<0.5	<0.5
Inhibitor (%)	IEC 60666	n/a	0.28	n/a

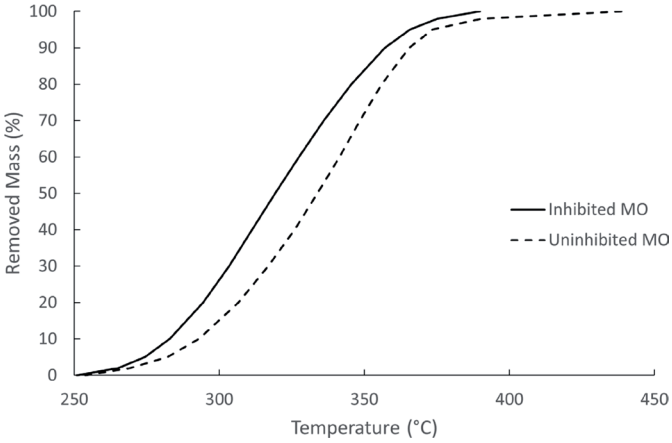

Fig. 1. Boiling Point Distributions for the two mineral oils according to ASTM D2887. Boiling point distribution data for the natural ester is unavailable.

DGA samples were collected via a dedicated sampling port in accordance with IEC 60475 [10]. Subsequently, the samples were sent to Bureau Veritas Commodities Antwerp NV, located in Antwerp, Belgium, for dissolved gas analysis following IEC 60567 [11].

B. THE EXPERIMENTAL SETUP

The assembled setup is modelled after a configuration presented by Wang et al. at Manchester University [7], and is described elsewhere [12]. Broadly, it comprises a 12-litre stainless-steel oil tank connected by a pipe that passes through a furnace, and then returns to the tank, forming a closed loop (Figure 2).

The heating section incorporates a pipe furnace featuring a 15 cm heated zone, capable of achieving a maximum operating temperature of 1200°C. The pipe that passes through the furnace is enveloped in a copper mantle to enhance heat dispersion and transfer efficiency. A hole in the mantle facilitates insertion of a thermocouple for measuring the outer surface temperature of the steel pipe. Additionally, another thermocouple measures the interior temperature of the pipe at the same position.

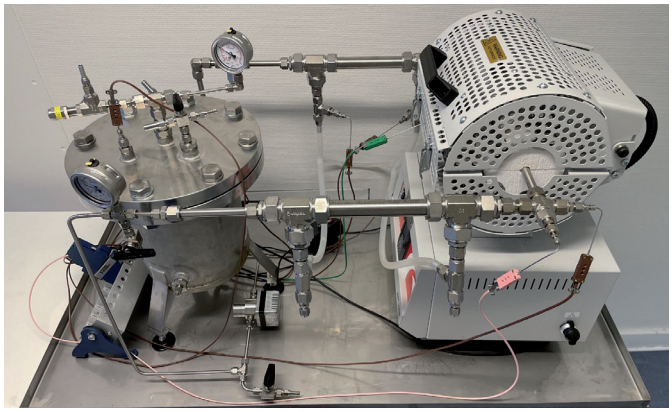

Fig. 2. Overview of the setup, including the tank, the pipe furnace, and the two water coolers before and after the furnace. The sampling port can be seen beneath the manometer attached to the pipe just before the inlet cooler of the furnace. An NI CompactDAQ chassis with a module for connecting eight thermocouples is visible in the lower left of the figure.

Throughout the experiment, temperature data is continuously collected from the thermocouples using a LabVIEW interface. Furthermore, temperature readings, target set points, and power levels from the furnace are continually logged. Pressures within the tank and the pipe are monitored through visual observation.

C. EXPERIMENTAL PROCEDURE

The analysis of dissolved gases in the three insulating liquids was conducted at three hotspot temperatures: 275°C, 550°C, and 800°C. These temperatures align with the T1, T2, and T3 thermal fault classifications as stipulated in IEC 60599. The duration of treatment was 168 hours, 6 hours, and 3 hours for the respective treatment temperatures of 275°C, 550°C, and 800°C.

When investigating a new liquid, it's necessary to replace the pipe that runs through the furnace with a fresh, unused pipe. The system is then pressurized to 1 bar above normal pressure for 24 hours to ensure proper sealing. Additionally, a level is employed to confirm that the pipe loop passing through the furnace maintains a horizontal orientation.

One 4L aluminium bottle is emptied into the clean tank, resulting in an 8L headspace within the tank. Upon activating the pump, the pressure is lowered to 0.2 bar. Subsequently, nitrogen gas is introduced to reach 1.0 bar. This pressure cycling is repeated for five cycles, achieving an oxygen content in the gas phase of less than 70 ppm. After this process, a blank DGA sample is collected from the sampling port while the pump operates at a low speed.

For the heat treatment, the pump is switched off, and the furnace's set point is adjusted to a suitable temperature, T_{SP}, that ensures the correct pipe temperature. Once the heat treatment concludes, the furnace is powered down and allowed to cool. To maintain consistency, the treatment duration is measured from when the furnace set point is set to T=T_{SP} until it is set to T=0°C. As the furnace's external pipe temperature reaches around 350°C, the pump is turned on at a low flow rate to expedite cooling. When the external pipe temperature dips below 100°C, a DGA sample is obtained. By this stage, the tank's temperature has risen to 30-35°C.

Pär Wedin, Elena Minchak, Carl Wolmarans, Robert Fairholm, Jessica Singh, Kaveh Feyzabi, Thomas Norrby, Simulated Thermal Fault: Assessing Dissolved Gas Analysis through Tube Heating Method on Mineral Oils and Natural Ester, Journal of Energy, vol. 72 Number 3 (2023), 29–33
https://doi.org/10.37798/2023723503

III. Results and Discussion

The temperature profile during a six-hour heat treatment of the inhibited MO is displayed in Figure 3. From the moment the furnace initiates heating, it takes just under an hour for the outer pipe temperature to reach the intended hotspot temperature. The outer pipe temperature remains stable from that point until the heating is terminated. However, the measurements clearly show that the temperature inside the pipe is notably lower and displays significant fluctuations. Temperature fluctuations are also evident at the furnace outlet and, to a lesser extent, at the furnace inlet. The deactivated pump effectively prevents backflow, allowing liquid to flow only to and from the tank via the furnace outlet. This explains the differences in temperature fluctuations between the furnace inlet and outlet.

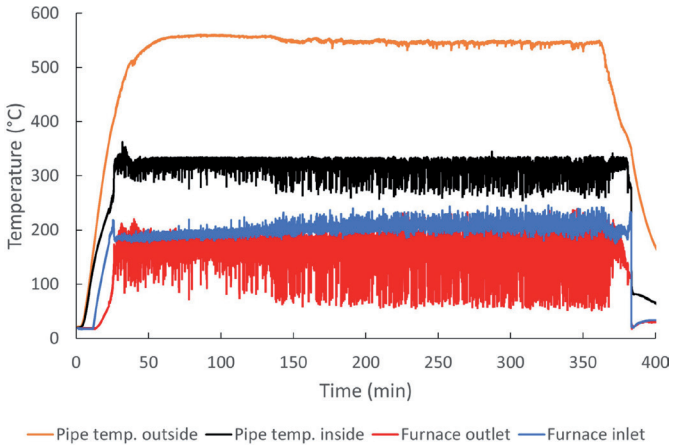

Fig. 3. Temperature profile of Inhibited MO run. Hotspot temperature corresponds to the outer pipe surface, and measurements are taken at the same location inside the pipe.

These temperature fluctuations stem from the evaporation of the MO within the furnace, causing hot gas to flow past the thermocouple at the outlet. As the hot gas reaches the cooler, it condenses, resulting in a pressure drop that compels cool oil to flow back past the thermocouple toward the furnace, as illustrated in Figure 4. This pressure drop is readily visible on the pipe's manometer and is often accompanied by an audible cracking sound emanating from the pipes. The temperature within the central section of the pipe, located inside the furnace, hovers around 325°C, corresponding to the midpoint of the boiling point distribution in Figure 1. Following the heat treatment, no discernible pressure buildup was observed within the tank. The temperature profile for the uninhibited MO exhibits analogous characteristics to that of the inhibited MO, differing primarily in the higher internal pipe temperature attributed to the elevated boiling point distribution.

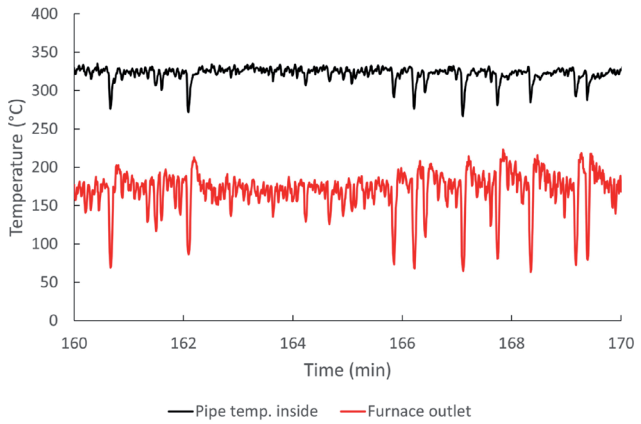

Fig. 4. Temperature fluctuations inside the pipe and at the furnace outlet for Inhibited MO.

The temperature profile for the natural ester significantly differs from that of the mineral oils, as depicted in Figure 5. Initially, the temperatures of the pipe's exterior, interior, and the furnace inlet and outlet steadily rise. However, around the 40-minute mark, the inner pipe temperature rapidly converges with the external temperature, and they remain virtually identical for the remainder of the heat treatment. Concurrently, the inlet and outlet temperatures decline

rapidly, approaching 44°C towards the conclusion of the heat treatment. During this period, the pressure within the tank also shows a notable increase of 0.2 bar, while maintaining an ambient temperature. With an 8L headspace, this pressure increment corresponds to a gas volume generated of 1.6L, significantly exceeding the volume within the pipes. This outcome likely signifies that, after approximately 40 minutes when the internal temperature reaches 340°C, the natural ester starts to decompose. The resulting gas evolution pushes the oil from the pipe into the tank.

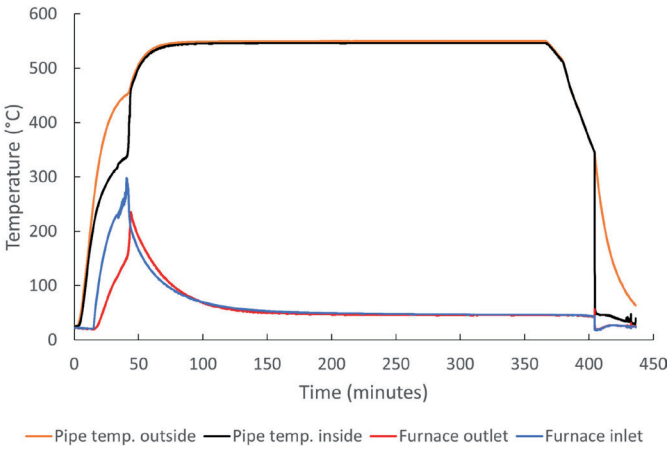

Fig. 5. Temperature profile during a typical run of the natural ester. The temperature profile suggests that the gas evolution during the thermal degradation of the oil has filled the pipe through the furnace with gas.

Some of the bulk properties of the oils were reanalysed following the 550°C heat treatment, and the results are presented in Table 2. The analysis of the key oil properties after the heat treatment reaffirmed the stability of mineral oil properties. Remarkably low DDF levels in the mineral oil samples indicate that even the uninhibited oil sample remained stable after the thermal treatment, preserving the oil's purity. Additionally, the low DDF levels provide confirmation that no contamination occurred during oil handling.

In contrast, the DDF level of the ester sample displayed a significant increase after exposure to the 550°C temperature, nearly four times higher than its initial value. This points to an elevated presence of polar contaminants, a consequence of fluid degradation. Furthermore, the deterioration of the ester oil is evident through a substantial increase in acidity attributed to the elevated quantity of fatty acids. The deterioration is further validated by a change in colour as per ASTM D1500.

Table II

Key Physical Properties of The Examined Insulating Liquids after Heat Treatment.

	Method	Uninhibited MO	Inhibited MO	Natural ester
Acidity (mg KOH/g)	IEC 62021-3	0.007	0.009	0.362
DDF at 90°C	IEC 60247	0.0002	0.0001	0.0399
IFT (mN/m)	ASTM D971	42.2	48.3	26.7
Color	ASTM D1500	<0.5	<0.5	0.8
Inhibitor (%)	IEC 60666	n/a	0.28	n/a

Pär Wedin, Elena Minchak, Carl Wolmarans, Robert Fairholm, Jessica Singh, Kaveh Feyzabi, Thomas Norrby, Simulated Thermal Fault: Assessing Dissolved Gas Analysis through Tube Heating Method on Mineral Oils and Natural Ester, Journal of Energy, vol. 72 Number 3 (2023), 29–33
https://doi.org/10.37798/2023723503

Table III

The Results from the Dissolved Gas Analysis for the Insulating Liquids. The treatment durations at different temperatures were 168 hours at 275°C, 6 hours at 550°C, and 3 hours at 800°C. The DGA analysis of the blank samples shows insignificant quantities of the gases of interest.

	Uninhibited MO			Inhibited MO			Natural Ester		
	w275°C	550°C	800°C	275°C	550°C	800°C	275°C	550°C	800°C
Hydrogen	<5	268	5788	<5	183	2374	<5	189	1973
Methane	1.4	1529	18961	2.7	1100	19175	2.2	1409	5481
Ethane	3.3	1722	15452	2.4	1432	16402	<1	7132	11349
Ethylene	2.3	1691	28333	1.2	1533	32774	1.5	11519	29285
Acetylene	<1	<1	54	<1	<1	65	<1	12	91
Carbon monoxide	<25	<25	<25	<25	<25	<25	95	1316	1741
Carbon dioxide	<25	68	96	39	108	73	434	5519	8956
Nitrogen	72238	25157	41045	75419	31226	40051	68769	26542	42471
Oxygen	2652	7399	8155	4428	8777	6923	29150	3869	2128
Total dissolved gasses	74914	37846	117892	79886	44379	117854	98451	57512	103473
Total combustible gasses	9.9	5222	68597	11.1	4269	70808	98.7	21584	49918

As presented in Table 3, the uninhibited MO exhibits higher concentrations of detectable key gases when compared to its inhibited counterpart at 550°C. However, the natural ester sample contains notably larger quantities of ethane, ethylene, carbon monoxide, and carbon dioxide. The increased presence of carbon monoxide and carbon dioxide can likely be attributed to the molecular structure of esters, signifying pyrolysis or molecular decomposition due to the elevated temperature. The amount of gas produced is at 800°C is significantly greater, but the trend is less clear. The uninhibited MO produces more hydrogen but less ethylene than its inhibited counterpart. The ester produces less methane and ethane than the mineral oils but still significantly more carbon monoxide and carbon dioxide.

IEC 60599 [9] recommends specific key gas ratios for determining the probable type of fault in a transformer through dissolved gas analysis, as detailed in Table 4. The calculated key gas ratios for the examined oils are presented in Table

5. In the case of a T1 thermal fault, the acetylene-to-ethylene ratio and the methane-to-hydrogen ratio is non-significant, regardless of their values. However, the ethylene-to-ethane ratio should remain below one. While this criterion remains applicable for both mineral oils, it is surpassed by the natural ester. Nevertheless, it's worth noting that the calculated key gas ratios offer limited relevance due to the extremely low concentrations of dissolved gases in all three insulating liquids.

Table IV

The DGA Interpretation Table for Thermal Faults From IEC 60599 [9].

Case	Characteristic fault	C_2H_2/C_2H_4	CH_4/H_2	C_2H_4/C_2H_6
T1	Thermal fault t < 300 °C	NS [1]	> 1 but NS [1]	< 1
T2	Thermal fault 300 °C < t < 700 °C	< 0.1	> 1	1 to 4
T3	Thermal fault t > 700 °C	< 0.2	> 1	> 4

[1] NS = Non-significant whatever the value.

Table V

Key Gas Ratios from DGA Of Insulating Liquids at Three Different Treatment Temperatures, According to IEC 60599.

	C_2H_2/C_2H_4			CH_4/H_2			C_2H_4/C_2H_6		
	275°C	550°C	800°C	275°C	550°C	800°C	275°C	550°C	800°C
Uninhibited MO	0.4	0.0	0.0	0.3	5.7	3.3	0.7	1.0	1.8
Inhibited MO	0.8	0.0	0.0	0.5	6.0	8.1	0.5	1.1	2.0
Natural Ester	0.7	0.0	0.0	0.4	7.5	2.8	1.5	1.6	2.6

At a hotspot temperature of 550°C, all three liquids exhibit negligible acetylene content. The methane-to-hydrogen ratio exceeds one, while the ethylene-to-ethane ratio falls within the range of 1.0 to 1.6. As per the guidelines outlined in IEC 60599, presented in Table 4, it is suggested that the three liquids have undergone a T2 fault condition. This observation aligns well with the pipe temperature of 550°C.

At an 800°C hotspot temperature, all three insulating liquids demonstrate a significant increase in gas generation. By the conclusion of the heat treatment, there was a noticeable rise in tank pressure—approximately 0.3 bar for the mineral oils and 0.7 bar for the natural ester. Consequently, the DGA samples exhibited a substantial presence of dissolved gases, as illustrated in Table 3. Post-heat treatment, a notable amount of carbonized oil residue remained within the pipe for all three liquids. This aligns with the description of a T3 fault in accordance with IEC 60599.

While acetylene content remains insignificant and the methane-to-hydrogen ratio exceeds one, the ethylene-to-ethane ratio falls below the expected value for a T3 thermal fault. As shown in Table 4, a T3 thermal fault should exhibit an ethylene-to-ethane ratio greater than four. However, the experimental results range from 1.8 to

Pär Wedin, Elena Minchak, Carl Wolmarans, Robert Fairholm, Jessica Singh, Kaveh Feyzabi, Thomas Norrby, Simulated Thermal Fault: Assessing Dissolved Gas Analysis through Tube Heating Method on Mineral Oils and Natural Ester, Journal of Energy, vol. 72 Number 3 (2023), 29–33
https://doi.org/10.37798/2023723503

2.6. Xing et al. [8] investigated simulated thermal faults on natural esters using a similar tube heating method, and also reported lower than expected key gas ratios. One plausible explanation for this discrepancy could be the composition of the pipe passing through the furnace, which is constructed from stainless steel, as opposed to the copper typically found in transformers. Another possible contributing factor to the discrepancy could be the relatively large head space in the tank. The lower solubility of ethylene compared to ethene in the liquid phase could also result in an artificially low ethylene-to-ethane ratio [3, 13].

IV. Conclusions

This study introduces a setup built upon the Tube Heating Method, designed to replicate thermal faults at very high temperatures. Samples can be conveniently obtained through a standard sampling port and sent for analysis. Moreover, due to the setup's use of readily accessible components, it can be easily adapted for integration with online DGA equipment.

The gas generation resulting from the investigating of an inhibited mineral oil, an uninhibited mineral oil, and a natural ester was carried out using the tube heating method, reaching temperatures of up to 800°C to simulate a hotspot. Both mineral oils produced similar quantities of gas. In contrast, the natural ester generated significantly higher amounts of carbon monoxide and carbon dioxide compared to the mineral oils.

When assessing the ratios of key gases, as recommended by IEC 60599, at 275°C, the generated gas levels were too low to reliably determine the likely fault type. At 550°C, all three liquids exhibited ratios indicative of a T2 thermal fault. However, at 800°C, the ethylene-to-ethane ratio was lower than expected for a T3 thermal fault. This difference could potentially be attributed to the use of stainless steel for the pipe material, as opposed to the copper commonly used in transformers, or to the comparatively large headspace.

References

[1] C. S. Narasimhan, *Transformer Oil – Application Aspects*. 2022, Zagreb, Croatia: Merit Media Int.

[2] N. Bakar, A. Abu-Siada, and S. Islam, *A review of dissolved gas analysis measurement and interpretation techniques.* IEEE Electrical Insulation Magazine, 2014. **30**(3): p. 39-49, DOI: 10.1109/mei.2014.6804740.

[3] C. Riedmann, et al., *Online dissolved gas analysis used for transformers – possibilities, experiences, and limitations.* e & i Elektrotechnik und Informationstechnik, 2022. **139**(1): p. 88-97, DOI: 10.1007/s00502-022- 00992-8.

[4] Y. Liang, et al., *New correlation features for dissolved gas analysis based transformer fault diagnosis based on the maximal information coefficient.* High Voltage, 2021. **7**(2): p. 302-313, DOI: 10.1049/hve2.12136.

[5] M. Jovalekic, D. Vukovic, and S. Tenbohlen. *Dissolved gas analysis of alternative dielectric fluids under thermal and electrical stress*. in *2011 IEEE International Conference on Dielectric Liquids*. 2011. DOI: 10.1109/ICDL.2011.6015457.

[6] L. Du, et al., *Studies on a Thermal Fault Simulation Device and the Pyrolysis Process of Insulating Oil.*Energies, 2018. **11**(12), DOI: 10.3390/en11123392.

[7] X. F. Wang, et al. *Dissolved gas analysis (DGA) of mineral oil under thermal faults with tube heating method*. in *2017 IEEE 19th International Conference on Dielectric Liquids (ICDL)*. 2017. DOI: 10.1109/ICDL.2017.8124635.

[8] Y. Xing, et al., *Difference analysis of dissolved gas in natural ester insulating fluids under typical electrical and thermal faults: An experimental study.* High Voltage, 2023, DOI: 10.1049/hve2.12338.

[9] IEC, *60599 - Mineral oil-filled electrical equipment in service - Guide to the interpretation of dissolved and free gases analysis*. 2022, International Electrotechnical Commission: Geneva, Switzerland.

[10] IEC, *60475 - Method of sampling insulating liquids*. 2011, International Electrotechnical Commission: Geneva, Switzerland.

[11] IEC, *60567 - Oil-filled electrical equipment - Sampling of gases and analysis of free and dissolved gases - Guidance*. 2011, International Electrotechnical Commission: Geneva, Switzerland.

[12] P. Wedin, et al. *Dissolved Gas Analysis on uninhibited and inhibited mineral oils and a natural ester under a simulated thermal fault using the Tube Heating Method*. in *2023 IEEE 22nd International Conference on Dielectric Liquids (ICDL)*. 2023. Worcester, Massachusetts, U.S.A., DOI: 10.1109/ICDL59152.2023.10209291.

[13] M. T. Imani, et al. *Measuring methods for solubility of gases in insulation liquids*. in *2017 IEEE 19th International Conference on Dielectric Liquids (ICDL)*. 2017. DOI: 10.1109/ICDL.2017.8124654.

ENERGIJA